Progress in Materials Science 123 (2022) 100839

Contents lists available at ScienceDirect

Progress in Materials Science

journal homepage: www.elsevier.com/locate/pmatsci

Cold-sprayed coatings: Microstructure, mechanical properties, and wear behaviour

Pedro Poza *, Miguel Ángel Garrido-Maneiro

DIMME – Durability and Mechanical Integrity of Structural Materials, Universidad Rey Juan Carlos, Escuela Superior de Ciencias Experimentales y Tecnología, C/ Tulipán s.n., 28933 Móstoles (Madrid), Spain

ARTICLE INFO

Keywords:
Cold spray
Microstructure
Mechanical properties
Nanoindentation
Wear
Erosion

ABSTRACT

Deposition of coatings on the surface of a bulk material is a versatile, economical, and effective strategy to provide additional features to the bulk material, mainly to improve its functionality and extend its service life. Among all the thermal deposition techniques, cold spray (CS) is the only technique in which particles are deposited below their melting point, and therefore, it is a solid-state processing technique. Coatings generated via CS exhibit different characteristics from those of the coatings produced by other methods; this may make CS a competitive technique for the repair and even for the manufacture of self-standing components.

This study presents a basic description of CS and a review of its applications in the deposition of metallic coatings, specifically those based on materials such as Al- and Ti-based alloys, used in aeronautical components. CS is a thermal spray technique that enables the production of coatings with properties and behaviours similar to those of bulk materials with similar compositions.

1. Introduction

Cold-gas dynamic spray or simply cold spray (CS) is a method used to deposit thick coatings or even freeform components and was developed at the end of the 20th century [1–5]. CS is a solid-state processing technique in which micrometre-sized particles are accelerated towards the substrate at relatively low temperatures. The driving force for material deposition is the kinetic energy acquired by the particles during acceleration to supersonic velocities. CS can be regarded as a new thermal spray deposition method, and powder melting is extremely rare in this technique. Due to the employment of low temperatures, CS demonstrates unique characteristics [6]. Microstructures and properties of the feedstock powders are retained, avoiding oxide formation or any other unfavourable structural changes, thereby increasing the durability of the coatings. Substrate–coating bonding and coating integrity are related to the plastic deformation of particles during impact. Adhesion of coating may occur in the solid state without significant damage to the substrate, even for temperature-sensitive materials. Although CS was initially used to deposit metals, nowadays, it is also employed to deposit polymers or ceramics including traditional and advanced materials.

CS deposition was discovered, partly by serendipity, at the Institute of Theoretical and Applied Mechanics at Novosibirsk, Russia, in the middle of the 1980s. The Russian researchers were studying two-phase flows for aerospace applications. In particular, they were performing wind tunnel experiments with gas–solid particle flows to investigate the influence of particles on the flow structure and their interaction with the model body [2,3,7]. In addition to achieving other results, the Russian research team realised that under

* Corresponding author.
E-mail addresses: pedro.poza@urjc.es (P. Poza), miguelangel.garrido@urjc.es (M.Á. Garrido-Maneiro).

https://doi.org/10.1016/j.pmatsci.2021.100839
Received 16 June 2020; Received in revised form 24 June 2021; Accepted 24 June 2021
Available online 28 June 2021
0079-6425/© 2021 The Authors. Published by Elsevier Ltd. This is an open access article under the CC BY-NC-ND license (http://creativecommons.org/licenses/by-nc-nd/4.0/).

some specific conditions, the fine Al particles, injected in a cold supersonic two-phase flow, deposited on the surface of the model body. This was the first time that a metal was cold-sprayed. With an increase in particle velocity, the effect of impact on the substrate shifted from erosion to the deposition of material on the target. The researchers identified this unexpected observation as a new phenomenon. The fundamentals of CS were established via new experiments and analyses. The first patents were presented by the group led by A.P. Alkhimov [8–10] at the end of the 1980s and the beginning of the 1990s. However, this process attracted the attention of researchers and companies around the world, and many patents were submitted in the following years [11,12]. At the beginning of the 21st century, a real commercial development of CS occurred, and the number of studies reported on CS exponentially increased [3,11]. Simultaneously, CS has been used in various technological applications. It has been applied to deposit protective coatings in many industries, such as aeronautics, automotive, mining, and power generation, to prevent damage to components and extend their service life [13–15]. Damage to components can be caused by chemical or mechanical interactions. The corrosion protection ability of CS-based coatings has been analysed [16–20], and several patents have been presented in this regard [12]. The abilities of Al- and Ti-based coatings to protect different components in industrial sectors, for example, aeronautics and biomedical, have been evaluated [21,22]. Ni- and Ni–Cr-based alloys [17,23,24] and other complex systems, including intermetallic compounds such as $TiAl_3$ [25], have also been considered for high-temperature oxidation protection. CS deposition of tribological coatings is slightly more complicated as metallic alloys are not the first choice for these coatings. Hard metals, ceramics, and composite materials are normally used to protect components against wear. The difficulties in the deposition of metal- and ceramic-based coatings have been overcome by using metal matrix composites (MMCs) and cermet coatings that are deposited by CS [23,15,26,27]. CS exhibits some advantages over traditional thermal spray methods [14] mainly because of its use of low temperatures. The content of oxides in the coatings deposited by CS is very low, extending their protective performance against corrosion. CS can be employed to deposit coatings on temperature-sensitive materials including Al alloys [28]. Finally, the level of residual stress induced by CS is substantially low, and typically, the coatings are in compression [29–33]. This enables the deposition of thick coatings, even up to several centimetres, without delamination or material cracking. This possibility has opened an interesting set of applications for CS, related to the restoration of components in several industrial sectors [34–36]. Among these applications, maintenance and overhaul of aeronautical components is significant as CS allows the deposition of coatings on temperature-sensitive materials, such as light alloys, that are extensively used in this industrial sector [26,37]. CS does not involve material melting. Therefore, the next step in the industrial development of CS is the processing of free-standing materials, which will lead to a new additive manufacturing technology with unique features when compared with those of traditional methods [36,38–40].

As mentioned above, the differentiating characteristic of CS as compared to those of other thermal spray processes is the employment of low deposition temperatures. This characteristic has broadened the range of applications of CS in systems where the use of high-temperature thermal spray techniques is not suitable, such as for the deposition of metallic materials on polymer substrates. Thermal spray deposition of metal particles on polymer-based structures has been extensively used to primarily improve the thermal and electrical properties, resistance to abrasion, erosion, maximum operating temperature, and the service life of polymer systems [13,41–44]. Some studies have been reported on the deposition of metallic coatings on polymer substrates using thermal spray techniques, where the particles are projected in the molten state. For the deposition of coatings on polymers, the use of flame spray, high-velocity oxy-fuel, or plasma techniques has been reported in literature because these techniques involve lower temperatures, thus minimising the thermal degradation of components [45–50]. For example, Voyer et al. [41] deposited Al on different polyester fabrics using flame spray. To obtain reliable coatings, it was necessary to cool the substrate to protect it from the high-temperature molten-sprayed metal or to increase the standoff distance between the substrate and the high-temperature molten-sprayed metal. Nevertheless, low deposition efficiencies were obtained. Consequently, the abovementioned deposition techniques exhibit two disadvantages: degradation of the polymer substrate and low deposition efficiency [51,52]. Degradation of the polymer substrate can be minimised using CS. Recently, studies on the application of CS in the production of metallic coatings on polymer substrates have significantly increased [44,51–58]. Zhang et al. [59] sprayed Al powder (99.7 wt% purity) with a nominal particle size range of $-75 + 15$ μm on substrates, including metals with different hardness values, polymers, and ceramics, via CS using He as an accelerating gas at room temperature (RT). Furthermore, acrylonitrile–butadiene–styrene copolymer (ABS) was selected as the polymer substrate. After CS deposition, they observed that few very small Al particles adhered to the ABS surface, which was disrupted by the impacting particles. The relatively hard Al particles caused deformation and tearing of the ABS surface, indicating that the deposition of Al particles on ABS was not successful. However, subsequent studies have succeeded in depositing reliable metallic coatings on polymer substrates. Lupoi et al. [52] investigated the ability of CS to generate reliable metallic coatings on polymers and composite materials. They sprayed commercial Cu, Al, and Sn particles on several polymeric materials (namely, a commercial blend of polycarbonate and ABS, polyamide-6, polypropylene (PP), and polystyrene) and a glass fibre-reinforced composite. They concluded that the specific weight of particles and critical spraying velocity determine whether erosion or deposition would occur on the substrate due to the impact of the sprayed particles. Additionally, higher deposition efficiency is expected when low-yield strength powders are sprayed on polymer substrates [44].

Ganesan et al. [60] sprayed two different Cu powders, that is, spherical and dendritic, and a spherical Sn powder on polyvinyl chloride and epoxy substrates. In their study, a commercially available cold gas technology (CGT) kinetic spraying system (Kinetics 4000, CGT, Germany) was used. N_2 gas was employed as the driving and powder feed gas. They observed that the metal particles did not experience any plastic deformation owing to the soft nature of the polymer substrates. Particles attached to the thermoplastic substrate through either adhesive bonding and/or mechanical interlocking, whereas only localised fracture was noticed on the thermosetting substrate, and thus, the particles did not firmly bind to this substrate. Thus, CS appears to be more successful for thermoplastics than for thermosets [61]. Consequently, the mechanical behaviour of the substrate influences the reliability of the coating and the bonding mechanisms. Additionally, the deposition of metal powders is affected by other parameters such as the

velocity and temperature of the impacting particles, roughness and temperature of the substrate surface, and relative angle between the particle trajectory and the substrate [62,63].

The application of CS in polymeric material systems can be further expanded to the deposition of polymeric materials on polymer substrates [64 65–67]. Bush et al. [64] studied the effects of the size, velocity, and temperature of particles and nozzle design on the deposition window and deposition efficiency of high-density polyethylene (HDPE) particles. These particles were sprayed on several polymer substrates. They reported deposition efficiencies of approximately 10% for the HDPE particles on soft low-density polyethylene substrates and slightly lower efficiencies in the case of other substrates. Ravi et al. [68] deposited ultra-high molecular weight polyethylene on Al and PP substrates. In their experiments, a thick coating could only be achieved using a 4 wt% alumina (Al_2O_3) nanoparticle additive to facilitate interparticle bonding. Shah et al. [67] showed that the addition of metallic nanoparticles to polymer particles improved the probability of deposition of polymer particles by increasing their density and impact kinetic energy for a fixed impact velocity.

Conventionally, when metals are cold-sprayed on metallic substrates, adhesion occurs by a combination of mechanical interlocking and metallurgical bonding via an adiabatic shear instability (ASI) mechanism [69,70], which has been comprehensively discussed in the subsequent section. However, for polymer substrates, the ASI mechanism may not be applicable. Shah et al. [67] also indicated that the adhesion mechanism of sprayed particles is based on localised particle melting. Nevertheless, other researchers have reported mechanical interlocking as the dominant adhesion mechanism for nearly all polymeric materials. Che et al. [56] proposed that CS on polymer substrates should be considered as a two-step process. The first step involves the development of the first layer, where the particle velocity must reach the onset velocity for particle/substrate interlocking. The second step is a build-up process, which is similar to the conventional CS deposition of metals.

By investigating the coatings generated in polymeric systems via CS, the activated adhesion mechanisms, properties of materials, and spraying parameters influencing the deposition of coatings have been studied. The stiffness relationship between the particle and the substrate affects the adhesion mechanisms. For soft (particle)/hard (substrate) systems, bonding and deposition of coatings are predominantly controlled by particle plasticity. In contrast, physical trapping and mechanical interlocking play important roles in hard (particle)/soft (substrate) systems [71]. Nevertheless, the corresponding deposition mechanisms are still under debate.

However, CS has some disadvantages as compared to other thermal spray techniques. The deposition of coatings using CS is based on the plastic deformation capacity of the particles and the substrate. Consequently, CS requires the substrates to have a minimum ductility to produce well-bonded coatings, limiting the ability of this technique to deposit coatings on ceramic substrates. Typically, in the as-sprayed condition, the cold-sprayed coating demonstrates higher hardness than that of the bulk alloy and thus lower ductility, which, in many cases, increases the requirement of a post-heat treatment.

Several books [2,4,5,72,73] and reviews [7,13,74–76] have been published on the fundamentals of CS deposition. Nevertheless, no comprehensive review has been reported on the mechanical behaviours and the micromechanisms responsible for the mechanical

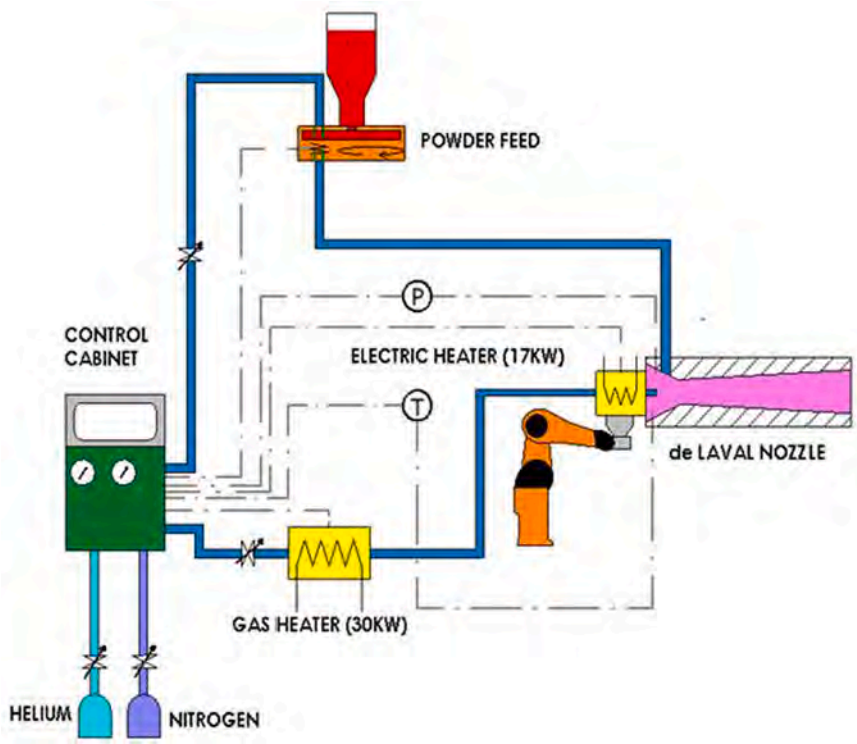

Fig. 1. Schematic of CS process. Reproduced from [24].

performances of cold-sprayed materials. However, the mechanical performances of CS deposits are a key factor for their industrial applications. This work considers cold-sprayed materials from the perspective of their mechanical performances including their tribological behaviours: scratch, dry wear, and erosion. Herein, the bonding mechanisms of CS deposits and the available CS devices have been briefly introduced. Subsequently, the microstructures, mechanical properties, and tribological behaviours of CS materials are discussed. Finally, the main conclusions of this review and the future trends for CS are presented. This review principally focuses on metallic materials, and the behaviours of Al and Ti alloys during the maintenance and overhaul of aeronautic structures have been comprehensively discussed.

2. Physics of CS bonding mechanism

CS is a solid-state deposition method that accelerates solid powder particles, with diameters between 1 and 50 μm, towards a substrate. The particles undergo significant plastic deformation upon impact, producing a coating or even a free-standing component. Powder particles are accelerated by the drag force exerted by a high-velocity gas jet. Carrier gas, which could be air, N_2, He, or their mixture, is split into a larger part of the carrier flow that is heated and a smaller part of carrier gas that remains cold. It is passed through the powder feeder and entrains a controlled powder flow to the nozzle. Then, the two carrier gas flows are combined and accelerated through a de Laval convergent–divergent nozzle. The particles acquire supersonic velocities, ranging between 300 and 1200 ms^{-1}, and their temperatures are maintained below their melting points. Fig. 1 shows a schematic of a general CS process [24]. The high plastic deformation induced in the powder particles at extremely high strain rates during impact promotes adhesion of the coating to the substrate [1,7,13,77,74,69].

Since the discovery of CS in the 1980s, it has been observed that powder deposition takes place only in a limited range of particle velocities [69,78]. The impact of particles accelerated at low velocities (<200 ms^{-1}) on a substrate is responsible for erosion processes similar to those noticed in micro-grit blasting or peening operations [77,79]. The larger-sized particles elastically rebound from the surface. Submicron-sized particles impacting the substrate may adhere to the substrate by van der Waals electrostatic forces; nevertheless, this cannot be considered as CS, which is characterised by strong bonding between the substrate and particles. Although few powders may be embedded, typically the substrate experiences net material losses because of erosion [77,79]. To overcome this situation, the particle velocity should exceed a critical value known as *critical velocity*, V_c. Above V_c, powder particles deposit on the substrate, and material gain occurs. Finally, if the particle velocity is increased to hyper velocities (>3000 ms^{-1}), impact stresses exceed the strength, and strong shock waves are developed. Under these conditions, a transition from deposition to severe erosion takes place. This transition velocity was calculated as *2Vc* by Schmidt et al. [78]. This limit is not easily maintained by the currently available CS devices. The development of CS systems is focused on accelerating the powder particles to obtain the maximum number of particles with velocity higher than *Vc*.

Particle velocity has been evaluated by fluid dynamic analyses [2,75,77,69,78,80–84], which is sensitive to several processing

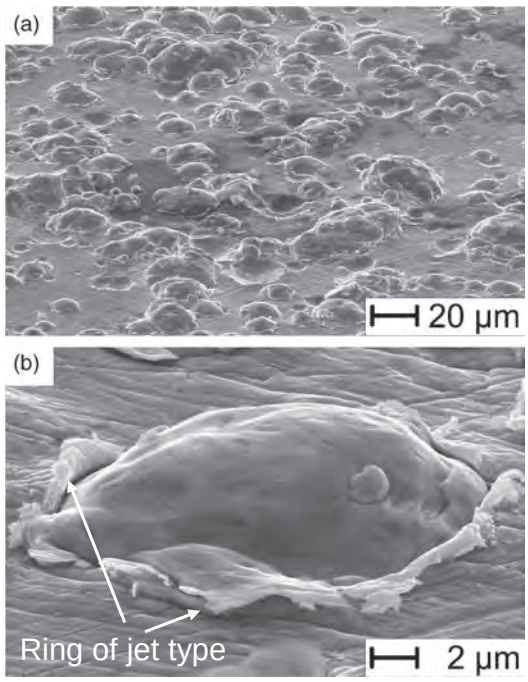

Fig. 2. SEM images of the Cu particles cold-sprayed on a Cu substrate. (a) Overview. (b) Detailed view showing jet formation. Reproduced from [69].

parameters such as the type of propellant gas, carrier gas pressure and temperature, nozzle design or standoff distance, and powder characteristics including size and shape. Particle velocity increases when He is used as the propellant gas; however, He is more expensive than N_2. Gas velocity and consequently particle velocity increase with an increase in temperature and pressure.

V_c has also been analysed, and it depends on not only the properties of materials (powder and substrate) but also the morphology and size distribution of the powder [2,77,69,78,80,81,83]. V_c increases with a decrease in powder size because smaller particles exhibit a higher area-to-volume ratio. However, large particles have higher inertia, and it is more difficult to accelerate them to high velocities [78,81]. Therefore, an optimum particle size range should be defined for each substrate–powder couple, and the particle diameters are usually between 10 and 45 μm [77,78].

Mechanisms responsible for CS adhesion are related to the high plastic deformation and high strain rates of the powder particles during impact. Comprehensive computational analysis has been conducted to examine the bonding between the particles and the substrate [74,81]. The most extended theory to justify CS bonding is the ASI mechanism, which is controlled by the plastic deformation of the particles with velocities above V_c. ASI occurs due to the combination of strain hardening during impact, attributed to the high plastic deformation developed on the powder particles, and softening induced by the heat released at the particle/substrate interface owing to high strain rate deformation during impact [7,74,77,69,81].

Bonding mechanisms have been experimentally and numerically studied. From an experimental point of view, the morphology of the impacted particles has been analysed using scanning electron microscopy (SEM) ([7,74,77,69,81]). Results show the formation of a ring with a jet-type morphology around the impacted particle bonded to the substrate (Fig. 2). In contrast, non-adhering particles leave a crater on the surface with no signs of jetting. The adhesion of the splats is controlled by the ductilities of the powder and the substrate. When the ductilities of the particle and the substrate are similar, both materials plastically deform. Deeper embedment is achieved using softer materials. If the powders are harder than the substrate, the powder particles will embed in the surface. Depending on the resistance of the substrate to embedment, the particles can be slightly or not at all deformed. Finally, if the powders are softer than the substrate, they will be mainly deformed and adhered to the surface.

CS bonding has also been evaluated by computational methods [74,80,81,85]. The impact of particles on the substrate has been examined using the Johnson–Cook (J–C) plasticity model, which considers the effects of strain hardening, high strain rate hardening, and thermal softening [74,85,86]. Analyses using other plasticity models have also been performed [74,87,70], and the J–C plasticity model has been found to be the most effective model for CS impact problems. Fig. 3 shows the evolution of the plastic deformation of the particle and substrate during impact [70]. The particle penetrates the substrate, developing a crater (Fig. 3(a)). The diameter and depth of the crater increase as the particle comes in contact with the substrate; simultaneously, the particle flattens, and its height-to-

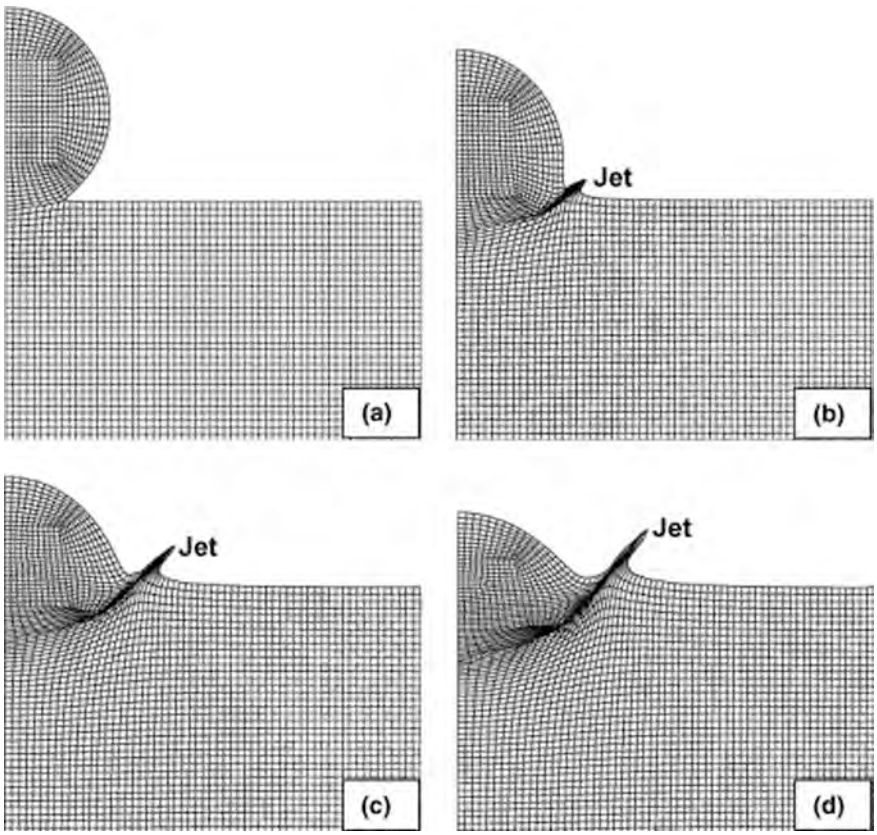

Fig. 3. Evolution of the plastic deformation of the particle and substrate during impact. Reproduced from [70].

width ratio decreases (Fig. 3(b), (c), and (d)). Plastic deformation occurs in a thin region close to the particle–substrate interface. Maximum plastic deformation is concentrated at the contact area border, where a jet of highly plastically deformed material is formed. These findings are in agreement with the experimental observations and validate the idea that the ASI mechanism is responsible for CS bonding. Jetting occurs due to the extrusion of material from the interface. The onset of ASI at the particle–substrate interface is considered a key factor in promoting the adhesion of particles to the substrate during CS. As mentioned above, two mechanisms compete. Owing to the high powder impact velocity, both the substrate and the particles plastically deform at very high strain rates, facilitating work hardening. With an increase in temperature, material softening occurs because of friction and dissipation mechanisms. Effective plastic deformation and temperature increase depend on the particle velocity and the initial particle temperature. Therefore, ASI takes place at a critical particle velocity, which is related to V_c [7,74,77,69,81,88–90].

The two main internal micromechanisms responsible for bonding are mechanical interlocking and metallurgical bonding, both of which can be activated by ASI [74,85,91]. Mechanical interlocking does not include any chemical reaction and involves mechanical trapping of particles by the substrate, resulting in a mutual geometric interlocking. In contrast, metallurgical bonding takes place via chemical reactions or diffusion at particle–substrate and particle–particle interfaces.

Although ASI is the most extended theory to explain CS bonding, other explanations have recently been proposed by Hassani-Gangaraj et al. [92–94]; nevertheless, there is some controversy [95]. These authors considered that jet formation is the key factor controlling the CS bonding and ASI is not necessary. In fact, jetting can be generated by the interaction of strong pressure waves with the free surface at the particle edges. This is a natural dynamic effect, which occurs when impact takes place with sufficient velocity. This process can promote hydrodynamic plasticity, which affects bonding without ASI.

3. CS devices

During the last few decades, numerous CS devices have been introduced in the market. All these devices accelerate the particles to high impact velocities using a pressurised propellant gas stream expanded in a de Laval (convergent–divergent) nozzle (Fig. 1) [1,77,96]. Typically, two approaches are employed to feed powder particles into the propellant gas flow. The first approach introduces the particles into the gas stream before the de Laval-type nozzle throat, where the gas pressure is higher than the environmental pressure. This process is used in high-pressure CS (HPCS) devices and is referred to as upstream injection. Powder particles are pushed into the gas flow under high pressure, and the system requires a powder feeder capable of operating under these conditions [1,2,77,96,97]. In the second approach, the particles are fed into the gas flow downstream of the de Laval-type nozzle throat. This process is used in low-pressure CS (LPCS) devices and is indicated as downstream injection [2,77,96–98].

Theoretically, any pressurised gas can be used for CS. However, commonly, air [99,100], N_2 [101–103], and He [83,104–106] are used [2,77,96]. N_2 and He are inert gases with obvious advantages for material processing. The use of light gases, such as He, with low molecular weights is more appropriate for CS as higher velocities of these gases can be attained using a de Laval nozzle. Consequently, He can be considered as the best candidate for propellant gas in CS deposition. However, He is extremely expensive and unaffordable for general use and is thus reserved for a few specific applications. He can be mixed with N_2; nevertheless, this will reduce particle velocities due to the higher molecular weight of the resulting mixed gas [107–109]. Therefore, N_2 is the most commonly used propellant in CS applications [2,77,96].

The de Laval nozzle design is critical for CS deposition as the conversion of a high-enthalpy, high-pressure, and low-velocity gas into a low-enthalpy, low-pressure, and high-velocity gas occurs through the nozzle. The objective of the nozzle design is to obtain a supersonic gas flow as highly favourable as possible for kinetic deposition. The gas stream should be able to transfer sufficient energy to the powder particles to impact and consolidate them at the substrate. The gas flow characteristics are controlled by the nozzle and gas parameters, primarily the type of gas, temperature, and pressure. The main features of the nozzle geometry are the divergence ratio, divergent shape, and diverging section length [2,96].

In downstream injection devices used in LPCS, air or N_2 is employed as the propellant gas under low or medium pressures (between 0.4 and 3.4 MPa), preheated to a maximum temperature of 550 °C. This gas flow is forced through the de Laval nozzle, reaching a supersonic regime with velocities of approximately 300–900 ms^{-1}. These systems are normally compact, portable, and inexpensive. However, the low pressures and temperatures used in these systems may limit the range of powders that can be deposited. Therefore, the maximum operating temperatures and pressures of these systems have been increased in recent years, expanding the range of materials sprayable via LPCS [98,110].

In upstream injection devices used in HPCS, N_2 or He is employed under high pressures, which can reach up to 7 MPa, and preheated to temperatures as high as 1100 °C. Similar to the case described for downstream injection, the gas flow is forced through the nozzle to be converted into a supersonic regime with velocities of approximately 1000 ms^{-1}. In this case, the powder is axially injected into the gas stream, upstream of the nozzle throat. Therefore, a high-pressure powder feeder is needed. The main advantage of these devices is the attainment of higher velocities when compared with those in the case of downstream injection devices. In addition, the powder particles can be preheated in the high–pressure section of the de Laval nozzle, reducing the required V_c. Both these effects promote the deposition of a wide range of materials. These facilities are more complex and expensive than LPCS devices and are not compact or portable. In the last few years, technology has been developed to achieve high particle velocities using N_2 [2,96].

Recently, CS deposition has been combined with laser technology to deposit materials with enhanced performance. Laser-assisted CS (LACS) involves laser pre-treatments of substrates before CS deposition to improve adhesion and to extend the range of materials that can be cold-sprayed. LACS includes both laser pre-treatment and CS deposition in one step [111–116]. Furthermore, laser post-treatments have been performed on CS coatings to improve their durability [117,118].

4. Microstructures of cold-sprayed materials

Cold-sprayed materials, processed using upstream or downstream injection, are produced by the deposition of particles in the solid state, as discussed above. Consequently, their microstructures are formed of splats, which are particles highly deformed owing to impact. A fine grain structure is normally formed inside the splats [23,119,120]. Fig. 4a depicts the splat microstructure obtained by Sirvent et al. [102] for Al 2024 cold-sprayed at 350 °C under 3.75 MPa using an HPCS device. A pancake morphology was generated by the splats with equiaxed grains inside them and elongated grains at their boundaries. The equiaxed grains inside the splats are shown in Fig. 4b. The formation of elongated grains at the splat boundaries indicates the high plastic deformation experienced by the powders during CS. The coating microstructure at the splat scale reveals the material homogeneity related to the build-up process as a function of powder characteristics.

CS deposition occurs in the solid state, and the phases in the original feedstock particles are typically preserved without oxidation or other undesirable reactions. The strain and heating rates can reach approximately 10^9 s^{-1} and 10^9 K s^{-1}, respectively [13,23,27,121,122]. These extreme conditions can promote grain refinement, strain accommodation, and interphase transformations that lead to different characteristic microstructures. Grain refinement takes place because of dynamic recrystallisation. After a particle impacts the substrate, intense shear stress deforms the impact region. Accordingly, recrystallisation initially takes place at the particle–particle interface. When ASI occurs, the material flows and dislocations entangle to form walls, networks, and finally subgrain boundaries [23,102,123]. The degree of recrystallisation and the size of the subgrains formed depend on the type of material and particle velocity. Therefore, CS parameters, including temperature and pressure, affect recrystallisation. Sirvent et al. [102] evaluated the effect of temperature on the CS deposition of Al 2024 by transmission electron microscopy (TEM) and observed that the subgrain size increased with an increase in the spraying temperature, suggesting the formation of less distorted microstructures in materials deposited at lower temperatures (Fig. 5).

Dynamic recrystallisation can be considered as a strain accommodation process. However, other mechanisms can also occur due to the high plastic deformation, and twinning is observed in materials with relatively low stacking fault energies. Strain can also be accommodated by solid-state phase transformation, which can facilitate the formation of amorphous and disordered structures [23,122,124]. These structures can affect the tribological behaviours of materials when the generation of mechanically mixed layers (MMLs) controls the wear mechanisms, as described hereinafter.

Interactions between particles or between the particles and the substrate during impact result in the generation of sub-micrometric structures at the splat interfaces or at the substrate–splat interface. These structures are formed under non-equilibrium conditions and may be important for controlling the adhesion and cohesion of the coating. Mechanical performances and integrities of the coatings are affected by these interactions, which can be classified into two categories: interactions contributing to local melting and those 'cleaning' the interface. Evidence of melting is difficult to obtain, and melting may be restricted to small interaction areas. Particle impacts and deformation might fragment or remove contaminants or particle oxide layers from the powder surface [23,120].

Due to the high plastic deformation induced in the sprayed particles during CS deposition, the coatings may exhibit high hardnesses, similar to that of a work-hardened alloy, with a high dislocation density. This increase in the hardnesses of cold-sprayed materials may affect their mechanical performances and tribological responses, specifically when the wear mechanisms are controlled by plastic deformation [23,102,123].

In general, fully dense coatings are preferred. Therefore, porosity is one of the microstructural features that is always analysed in CS materials. Porosity is attributed to insufficient particle kinetic energy or insufficient plastic deformation produced during impact. Porosity is normally observed at the splat interface and on the coating surface [23,119,125]. With an increase in particle velocity, porosity decreases. Parameters such as pressure and temperature should be carefully controlled to optimise the amount of porosity in CS materials. Fig. 6 depicts the optical images of the evolution of porosity in stainless steel 316L deposited by CS using an HPCS device at 900 °C under 5, 6, and 7 MPa [126]. It can be seen that porosity reduces with an increase in pressure.

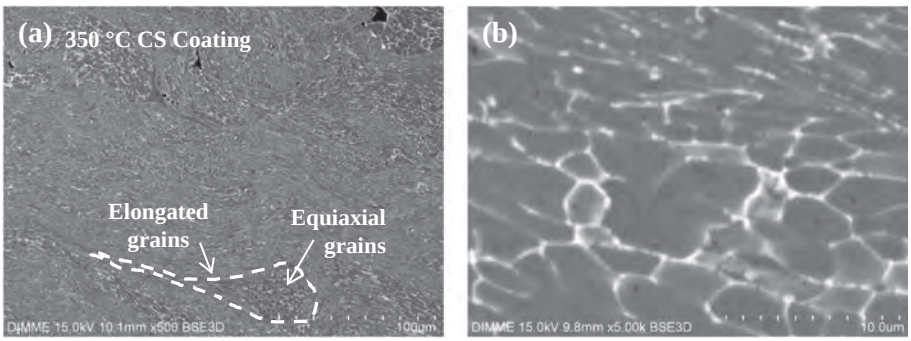

Fig. 4. Al 2024 cold-sprayed coating deposited at 350 °C under 3.75 MPa. (a) Splat structure showing different grain structures inside the splats and at the interface. (b) Equiaxed grains at the centre of the splats. Reproduced from [102].

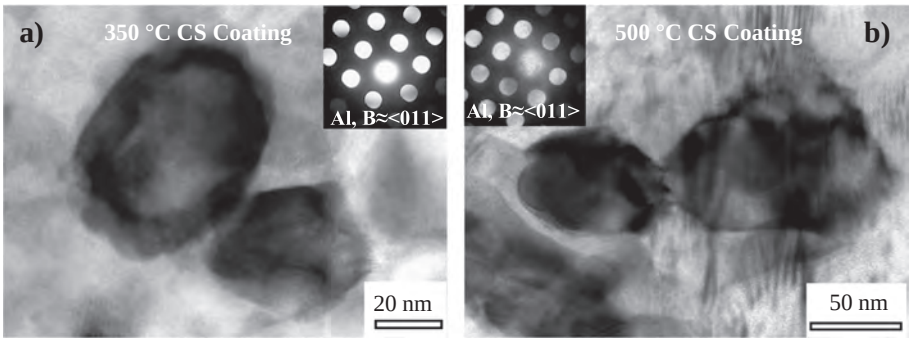

Fig. 5. TEM images of the subgrains formed in the Al 2024 coatings deposited by CS using 3.75 MPa at (a) 350 °C and (b) 500 °C. The subgrain size is clearly reduced at lower temperature. Reproduced from [102].

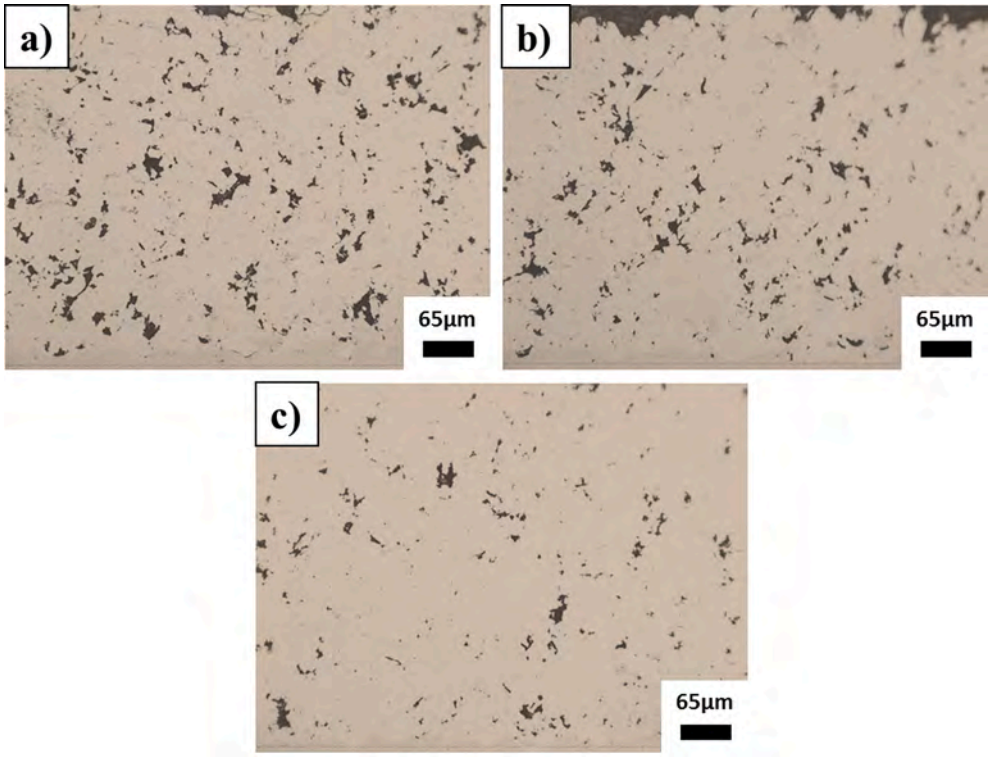

Fig. 6. Optical images showing the evolution of porosity in stainless steel 316L cold-sprayed at 900 °C under (a) 5, (b) 6 and (c) 7 MPa. Reproduced from [126].

5. Mechanical properties of cold-sprayed materials

Among various factors, reliability of a coating depends on its mechanical properties. A key property that determines the functionality of a coating is the adhesion of the coating to the substrate on which it is deposited.

Adhesion strength between the coating and the substrate can be investigated by the pull test described in the ASTM C633 standard [127]. In this method, tensile stresses are applied to a coated system consisting of a coated sample glued to another sample or insert (Fig. 7). A load is placed perpendicular to the coating–substrate interface. The level of tensile load is gradually increased from zero to the load that results in sample failure, that is, the coating fractures or detaches from the substrate. The coated surface is always a flat circle, and the sample dimensions are standardised. The bond strength is calculated as the load at the sample failure divided by the coating failed area. Occasionally, failure occurs in the adhesive used to bond the coating to the insert. In this case, the measured resistance value constitutes a threshold value of adhesion between the coating and the substrate.

There are two main strategies to improve the adhesion between the coating and the substrate. In the first strategy, the surface roughness of the substrate is modified or a specific texture that improves the adhesion of the first sprayed particles to the substrate is

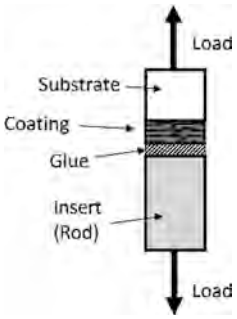

Fig. 7. Scheme of the pull test according to ASTM C633 standard.

generated [128,129]. In CS, coating is developed by the plastic deformation of particles; therefore, a significant influence of surface roughness on the adhesion is expected. Nevertheless, this is not always true and depends on the ability of the particles to deform and adapt to the surface texture of the substrate. The other strategy involves the optimisation of spraying conditions [130].

Perton et al. [131] investigated the effects of initial surface roughness, pulsed laser ablation (PLA), and laser preheating on the adhesion strength of cold-sprayed Ti-6Al-4V deposited on the substrates of the same alloy by an HPCS device. Adhesion strength was evaluated by metallographic examinations, laser shock technique (LASAT), and ASTM C633 pull tests. Surface finish of the substrates before CS was achieved using four different methods: (i) grit blasting with grit 24 or 100 Al_2O_3, (ii) an as-machined method, (iii) grinding with grit 400 or 800 SiC papers, and (iv) mirror polishing. PLA is employed in thermal spray to remove surface oxide and hydroxide layers as well as other contaminants from the substrate surface. In this study, this technique was performed prior to coating deposition to provide a fresh metallic surface for the impacting particles. Spraying was conducted using N_2 as the propellant gas and a gas temperature and pressure of 800 °C and 4 MPa, respectively. Standard ASTM C633 adhesion strength tests consisted of gluing the cold-sprayed samples to grit 24 alumina-blasted mild steel cylinders with FM1000 epoxy glue. The LASAT technique is based on the propagation of high-amplitude ultrasonic waves that provide a local measurement of joint strength. This strength is determined by increasing the laser pulse energy until debonding occurs. Highest adhesion strength of the Ti-6Al-4V cold-sprayed coatings was acquired on the mirror-finished substrates. Upon increasing the substrate surface roughness, a higher surface contact area was achieved for adhesion; however, the adhesion strength of the coating lowered due to the low deformability of the cold-sprayed Ti-6Al-4V particles, which decreased the ability of the sprayed particles to fill the asperities created by the roughening procedure. PLA had a negative effect on the adhesion of the deposited coating probably because of the interaction of the laser beam with the deposited particles. Finally, laser preheating enhanced the adhesion strength of the coating only when it was combined with PLA.

Although most materials can be easily deposited at relatively low deposition velocities (<700 m/s), higher deposition velocities are required for the deposition of high-yield-strength materials such as Ti or Ni and their alloys. Goldbaum et al. [130] analysed the effects of deposition velocity, powder size, particle position in the gas jet, gas temperature, and substrate temperature on the adhesion strength of the cold-sprayed Ti and Ti6Al4V splats deposited by HPCS. The adhesion strength between the splats and the substrate was measured by applying a normal force (F_N) of 30 or 300 mN to a stylus placed on the substrate. Then, the substrate was moved at a rate of 150 μm/min below the stylus. The adhesion strength of the splat was calculated via the relationship between the tangential force, F_T, exerted on the stylus and the splat area, A. They concluded that the combination of high velocities (1140 m/s) and preheating of the powder and substrate (400 °C) may be a key to the deposition of Ti6Al4V with high adhesion strength, approaching that of the bulk material.

Another property that describes the quality of the cold-sprayed coating is the cohesion or bonding between splats, which has been

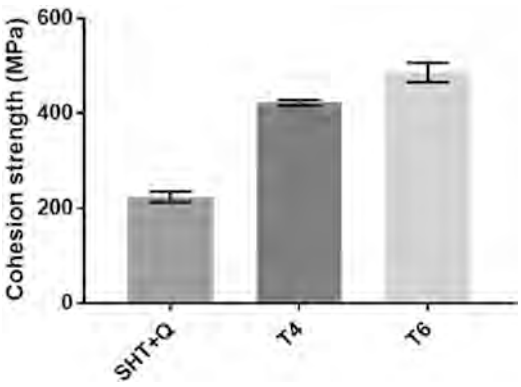

Fig. 8. Cohesion strength of the coatings sprayed using Al 7075 powders with different heat treatment and degrees of ageing. Reproduced from [129].

used to optimise the spraying conditions of the coating [78]. In the tubular coating tensile test (TCT test), two cylindrical substrates are fixed face-to-face by a screwable holder, which is later attached to a lathe chuck. The substrates remain in this fixed position during preparation and coating. The prepared substrates are radially and axially coated. The specimens are pulled after being unscrewed from the holder. The tensile force is continuously recorded until the coating fails. The cohesion strength can be measured by the relationship between the tensile force and the cross-sectional area of the coating.

Sabard et al. [129] sprayed Al 7075 gas-atomised powders using heated N_2 at 500 °C under 6.0 MPa in an upstream system. Before spraying, the powders were heat-treated, quenched, and subsequently aged by natural ageing at RT for 21 days (T4 treatment) and by artificial ageing at 120 °C for 24 h (T6 treatment). They evaluated the cohesive strengths of the coatings sprayed using heat-treated and quenched (SHT + Q), T4-aged (T4), and T6-aged (T6) Al 7075 powders by TCT tests. Fig. 8 shows the cohesion strengths of the coatings sprayed using SHT + Q, T4, and T6. The cohesion strengths of 224, 422, and 486 MPa were obtained for the coatings sprayed using SHT + Q, T4, and T6, respectively. This result implies that the cohesive strength gradually increases with ageing.

Another variable that has a significant influence on the cohesion strength of cold-sprayed coatings is the spraying velocity. The correlation between the cohesion strength and the impact velocity has already been investigated for Cu [81] and Ti [132]. In both studies, the effects of different spraying velocities of particles of different sizes on the cohesion strength were evaluated. Variation in the cohesion strength with an increase in impact velocity primarily depended on the particle size of the respective powder. However, variation in the cohesion strength with the ratio of the particle impact velocity to V_c appeared to be identical for all the examined powders. Nevertheless, the cohesion strengths of the cold-sprayed coatings seem to depend on the combined effect of the different spraying parameters.

In addition to the adhesion and cohesion of the coating, other properties, including elastic modulus (E) and hardness, are important to predict the behaviour of a coating. However, different test methods as compared to those used for the bulk material may be needed to determine these properties of coatings. Nanoindentation allows the evaluation of E and hardness and is suitable for analysing the mechanical properties of coatings. In nanoindentation, the material is indented by a tip with a known geometry during a loading and unloading cycle. During this cycle, the load and penetration depth of the indenter are continuously recorded to acquire force–displacement data [133].

It is expected that most of the variables of CS will have an influence on the properties of the coatings. Nanoindentation enables the discrimination of the effect of each variable on the mechanical properties of the coating, such as hardness. Nanoindentation has been used in several studies to characterise the mechanical properties of cold-sprayed materials [102,117,125,30,134–136].

Sirvent et al. [102] evaluated the effects of temperature on the quality and properties of Al alloy 2024 coatings deposited by CS using an HPCS device. The coatings were sprayed at a conventional temperature of 350 °C and at a non-conventional temperature of 500 °C on Al 2024-T351 substrates. Instrumented indentation tests were conducted on the substrate, particles, and cold-sprayed coatings to determine E and hardness. No considerable difference was noticed between the elastic moduli of the substrate, particles, and coatings. However, the hardness of the particles was lower than that of the substrate and coatings.

Garrido et al. [136] investigated the mechanical responses of Ti6Al4V coatings deposited on bulk Ti6Al4V using HPCS. Instrumented indentation tests were performed on the particles and the substrate. The hardness of the sprayed particles was significantly lower than those of the coatings and the substrate. Furthermore, the sprayed coatings showed higher hardness than that of the substrate. They attributed this increase in hardness to the high plastic deformation and work hardening of particles during deposition.

Tan et al. [137] studied the effects of coating thickness on the microstructures and mechanical properties of Ti6Al4V coatings deposited on Ti6Al4V substrates. The coatings were deposited using N_2 gas at 1100 °C. The deposition velocity was approximately 800 m/s. Prior to deposition, the substrate was heated to 200–300 °C for better adhesion. Ti6Al4V coatings with final thicknesses of 0.1, 0.5, 1, and 3 mm were analysed. They reported an increase in hardness near the interface, caused by the peening or hammering effect of the particles during coating build-up. However, at distances farther from the interface, the hardness was similar to that of the substrate.

Goldbaum et al. [138] examined the effects of spraying velocity on the mechanical properties of cold-sprayed Ti splats and coatings by nanoindentation. They reported that the average hardness of the cold-sprayed Ti splats remained similar at all deposition velocities and was higher than that of the feedstock material. The same behaviour was observed for the cold-sprayed coatings, whose mechanical properties remained constant across their cross-section thicknesses.

Bhattiprolu et al. [139] measured the nanohardnesses of Ti6Al4V powders manufactured by different techniques: gas atomisation, plasma atomisation, and hydride–dehydride (HDH). They reported that plasma-atomised and HDH powders exhibited higher nanohardnesses than that of the gas-atomised powders. They concluded that this difference in hardness was related to the microstructure and O content of powders. Microstructures with higher contents of α′ phase showed higher hardnesses. Additionally, the higher the O content, the higher the nanohardness of the Ti powder [140].

Campbell et al. [141] studied the deformation behaviours of Al-Al_2O_3 cermet coatings deposited by LPCS on AZ31 Mg and Al6056 lightweight alloy substrates by nanoindentation. They proposed a methodology based on the experiments and simulations of nanoindentation tests for estimating the coating yield stress. Several other studies were conducted on the evaluation of nanoindentation stress–strain curves [142–146].

Cortés et al. [147] investigated the effects of the spraying temperature and pressure on the mechanical behaviours of 316L stainless steel coatings deposited on C steel by CS. The spraying gas temperatures of 800, 900, and 1000 °C and gas pressures of 5 and 6 MPa were employed. Nanoindentation was used to obtain the stress–strain curves of the coatings. A Berkovich diamond indenter with a nominal tip radius of 20 nm and two spherical diamond indenters with nominal radii of 5 and 500 μm were utilised to characterise E and the stress–strain curves, respectively. Indentation stress–strain curves demonstrated an initial linear tendency, corresponding to the indentations conducted using the spherical indenter with a radius of 500 μm. These curves transitioned to a second nonlinear zone,

attributed to the indentations performed using the spherical indenter with a radius of 5 μm. They reported that this zone represented the plastic response of the coating. They concluded that the higher the spraying temperature and pressure, the more displaced the plastic branch towards higher stresses, and consequently, the higher the strain hardening because higher deposition temperatures and pressures facilitate the plastic deformation of particles during impact.

Owing to the versatility of the indentation technique, it can be applied to analyse the mechanical behaviours of polymer and polymer matrix composite systems. Serena et al. [71] reported nanoindentation measurements of the cold-sprayed coatings of steel and Al deposited on PP reinforced with C and glass fibres. Nanoindentation tests were conducted to determine the influence of the fibres and sprayed powders on the behaviours of the coatings. They observed that the coated specimens exhibited different shapes of the loading indentation branch depending on the sprayed material, number of passes, and the area where the tests were performed. Additionally, they reported a correlation between the morphology of the indentation loading curve and E and hardness values of the coatings. Viscusi et al. [148] studied the bonding mechanisms and the adhesion/cohesion strength of an alloy coating (AlSi10Mg) deposited on PP substrates by CS. Mechanical properties of the coating were determined via microindentation and conventional dynamic mechanical analysis tests. They reported that CS can be an effective technique to develop a reliable Al film on PP thermoplastics. They also concluded that the deposited Al film increased the stiffness and E of PP substrates.

Instrumented indentation can also be employed to analyse the damage mechanism of the coatings deposited by CS. A main failure mechanism of structural and moving components is the wear caused by friction or erosion. Determining the wear mechanisms and wear resistance is important to evaluate the service life of a component. Comparing the mechanical properties of the unworn and worn coatings may be of interest in understanding the wear process. Mechanical properties of the unworn coating and the residual wear track may be investigated by nanoindentation [149]. Furthermore, most nanoindentation equipment can be used to conduct scratch tests at different indenter velocities and loads. Therefore, this equipment may provide valuable information for analysing the tribological behaviours of cold-sprayed coatings.

6. Tribological behaviours of cold-sprayed materials

Analysing the mechanical properties of cold-sprayed coatings is essential to evaluate and predict the behaviours of these coatings under different solicitations. Nevertheless, in some situations, the mechanical responses of these coatings depend on not only their intrinsic properties but also the operating conditions under which these coatings work during their service life. In the case of the wear behaviour, temperature, material of the counterbody, loads, type of relative movement between the surfaces in contact, and surface roughness influence activation of the mechanisms responsible for wear. Therefore, wear resistance is not an intrinsic property of coatings or bulk materials. Consequently, to investigate the wear behaviour of a coating, it is necessary to first identify the operating conditions of the service in which it works. Therefore, the wear tests should be designed to simulate an arrangement significantly similar to a real arrangement. As mentioned in the Introduction section, one of the most important applications of CS is in the maintenance and overhaul of aeronautical structures.

CS is a promising cost-effective and environmentally friendly technique that offers surface protection, repair, and dimensional

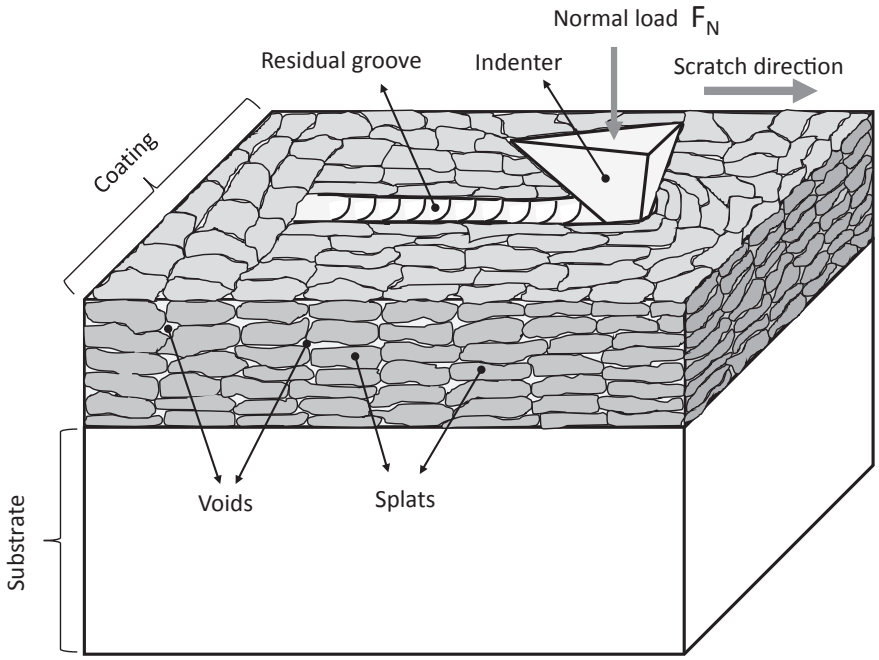

Fig. 9. Schematic of the scratch test.

tolerance restoration abilities to Mg, Al, and Ti alloy components used in aeronautics [4,26,37]; for example, helicopters and fixed-wing aircraft [150].

Stoltenhoff and Zimmermann demonstrated the potential of CS as a repair technique using three different precipitation-hardened Al alloys (AA2224, AA6061, and AA7075) in CH-53 helicopter landing gear shock struts and C-160 aircraft propeller blades [80,151]. Kumar et al. [152] reported the successful repair of Al and Mg aerospace components such as the S-70 Seahawk and C-160 Transall propeller blade using CS. For both applications, erosion was described as the primary wear process. Additionally, Kumar et al. [152] utilised CS to repair gas turbine components, including 6061 Al fan casings, susceptible to damage by friction and erosion.

In airframes, Ti6Al4V alloy is used for general structural materials, bolts, seat rails, and similar components. Due to the relatively low allowable temperature of approximately 300 °C in engines, the Ti6Al4V alloy is employed in fan blades, fan cases, and similar components in the intake section where temperatures are relatively low (600 °C or lower). During routine flight, the aircraft skin and components suffer from erosion and scratch damages owing to the high-velocity impact of dust and debris [36]. In these applications, CS can be used as a repair technique. Therefore, in the fabrication of Ti compressor case isogrid, CS is employed to develop areas to minimise the starting stock material and machining waste [36]. However, in many aeronautical applications, coatings are deteriorated by the wear damage caused by micro-scratches and the erosion of fine particles.

Accordingly, study of the wear response of the coatings deposited by cold spraying these alloys is of special relevance. Because CS is utilised for both the manufacture and repair of components, it is important to ensure that the spraying conditions generate a coating with wear resistance similar to that of the bulk material replaced by the coating. To achieve this goal, wear experiments should be conducted under different test conditions at different scales.

6.1. *Local wear behaviour: Scratch tests*

Over the past few years, scratch test has become a common method to determine the adhesion strength between the coating and substrate [153–159]. Furthermore, this test enables the characterisation of the wear rates of a coating on a local scale, where the wear response of a small volume of material is obtained [160]. Therefore, the wear resistances of the different phases present in a coating microstructure can be examined using this test.

Scratch tests of the coatings (Fig. 9) consist of a diamond stylus moving over the coating surface under a normal force. When the adhesion of coating/substrate systems is analysed via the scratch test, the normal force is increased either stepwise or continuously until coating failure occurs. Subsequently, this critical normal force (F_c) is taken as a measure of adhesion strength. The onset of coating failure is revealed by a sudden increase in the friction force and acoustic emission, which can be monitored by optical microscopy,

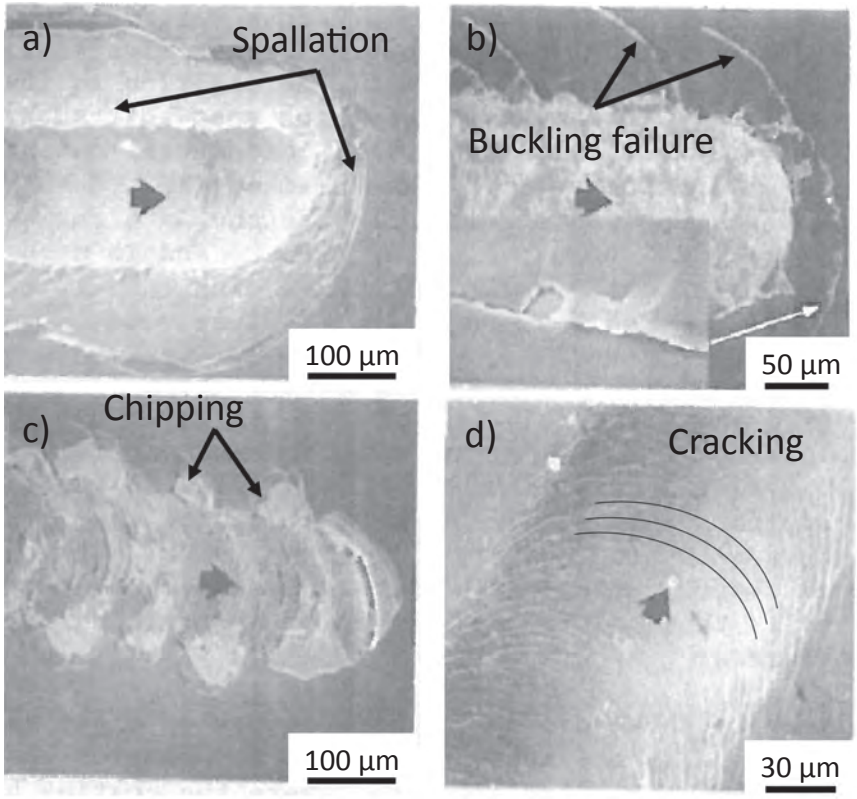

Fig. 10. Representative images of coating/substrate failure modes determined by the scratch test in plain view. Reproduced from [162].

acoustic emission, and friction force measurements [153,155]. The procedure of scratch test for testing the adhesion and cohesion strengths is described in the European Standard prEN 1071-3 [161]. In this standard, the coating, geometry, and material of the indenter and scratch test parameters, including loading rates and indenter transverse speed, are specified.

Scratch tests can also be used to determine the wear behaviours of coatings. Wear rates and mechanisms can be determined by measuring the coefficient of friction (COF) and analysing the residual grooves.

As can be inferred from the recommendations established in the prEN 1071-3 standard [161], the wear behaviour of a coating depends on several factors such as the tribological response. These factors can be related or unrelated to the coating. Factors such as i) the ratio of coating-to-substrate hardness, ii) thickness of the coating, and iii) surface roughness may be classified as the main factors related to coating. In contrast, factors including iv) geometry of the contact between the stylus and coating surface, v) scratch velocity, vi) force applied on the stylus, vii) surface roughness of the stylus, viii) stylus hardness, and ix) chemical affinity between the coating and stylus are related to the scratch test. Consequently, the wear mechanisms and their contribution to the tribological process depend on the abovementioned factors.

Failure mechanisms represent processes that lead to the detachment of coating when the critical force (F_c) is reached. These processes may be classified into plastic deformation, cracking, spallation, and buckling [162,163] (Fig. 10). When the critical load is reached, two different types of failures can be observed: brittle and ductile. Ductile failure is generally noticed in the case of ductile substrate materials, whereas brittle failure is observed for brittle substrates. However, both failures show many similarities, and differences are noticed in the areas affected by failure extension. To examine the critical adhesion strength between a coating and a substrate via scratch tests, coatings with thicknesses less than 20 μm are preferred [161].

During the investigation of the friction and wear mechanisms of the coating, a constant normal force at a specified scratch velocity is generally imposed on the coating surface during the test. Tangential force, scratch distance, and groove depth are continuously recorded during the test. Thereafter, the residual groove geometry is determined by the transverse profiles of the scratch tip or by profilometers. The tangential force is utilised to analyse the COF, and the residual groove geometry is used to evaluate the removed volume and thus the wear rate. As mentioned above, a diamond stylus is normally used in scratch tests. Consequently, the chemical affinity between the stylus and the material being scratched and the adhesive transfer feature of the adhesive wear process are limited. Additionally, the stylus is typically harder than the surface. Therefore, a single contact point model can be speculated, where a hard, sharp abrasive is indented against the flat surface, which forms a groove on the surface by ploughing. Thus, ploughing that occurs when the stylus scratches the surface material can be considered. Owing to ploughing, a certain volume of surface material is removed, and an abrasive groove is produced on the surface. This type of wear is called abrasive wear [164]. Processes through which the material is removed by ploughing depend on the mechanical behaviour of the material being scratched. When the wearing material has a ductile property, a ribbon-like, long wear particle is developed via two basic mechanisms: a cutting mechanism and a wedge build-up mechanism with flake-like debris [165]. The wedge build-up mechanism is known as ‘ploughing’, and the cutting mechanism is called ‘micro-cutting’. Ploughing is a less efficient mechanism of metal removal than micro-cutting. Fig. 11 depicts a schematic of the scratch process of a ductile material, where the effects of ploughing and micro-cutting mechanisms are outlined.

In the case of a brittle material, wear is mainly generated due to brittle fractures caused by the initiation and propagation of cracks, such as median and lateral cracks. Therefore, the wear rate of brittle materials substantially depends on fracture toughness. Fig. 12 shows a schematic of the scratch test of a brittle material.

6.1.1. *Scratch test: Adhesion strength measurement*

To measure the adhesion strength of coating/substrate systems by the scratch test, the diamond stylus is moved over the surface of

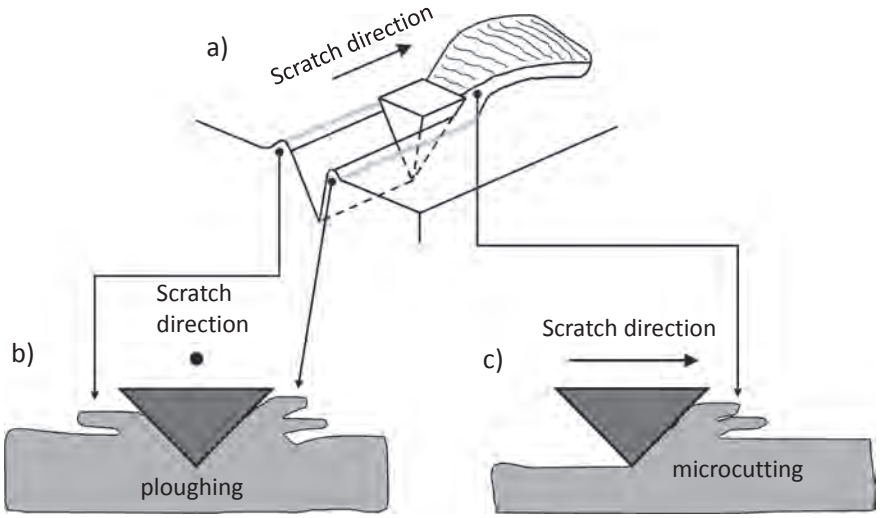

Fig. 11. Schematic diagram of the scratch process onto a ductile material. (a) General view; (b) Ploughing effect; and (c) Micro-cutting effect.

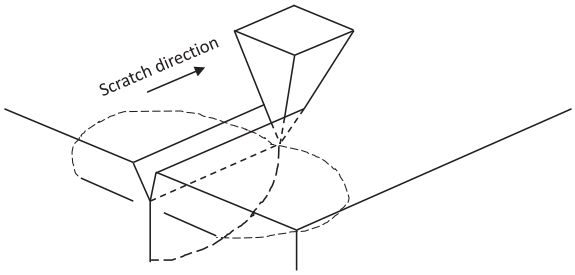

Fig. 12. Schematic of the scratch process onto a brittle material.

the sample under a normal force, which is increased until a critical normal force is reached, where a well-defined coating failure occurs. This force is related to the adhesion between the coating and the substrate. Consequently, several models have been proposed to predict adhesion strength from critical load. Note that coating adhesive failure is directly associated with a sudden increase in the friction force [153,155,156]. Therefore, the COF or tangential force should be continuously recorded during the scratch test. In general, higher values of COF correspond to lower critical loads [157]. Therefore, an inverse relationship is expected between the adhesion models of both these parameters.

To evaluate the adhesion strength, two main approaches have been proposed. In the first approach, adhesion is measured through the shear strength, whereas in the second approach, it is estimated by the strain energy released during the removal of the coating.

Benjamin and Weaver [166] proposed the following equation to calculate the frictional force per unit area of the coating (σ_τ):

$$\sigma_\tau = \frac{KaH_s}{\sqrt{(R^2 - a^2)}} \tag{1}$$

where R is the indenter tip radius, a is the radius of the circle of contact, Hs is the indentation hardness of the substrate, and K is a constant varying between 0.2 and 1.0 [159,166]. a can be related to F_c via Eq. (2) [167]:

$$a = \sqrt{\frac{F_c}{\pi H_s}} \tag{2}$$

By substituting Eq. (2) into Eq. (1), a relationship between σ_τ and critical load, Fc, can be obtained.

Laugier [168,169] suggested that the adhesion behaviour of a coating can be modelled using the strain energy released during the removal of the coating. The following equation was proposed by Laugier [169]:

$$\omega = \frac{\sigma_\tau^2}{2E_c} t \tag{3}$$

where ω is the work of adhesion, t is the thickness of the coating, E_c is the Young's modulus of the coating, and σ_τ is the stress responsible for the detachment of the coating ahead of the indenter.

To relate ω to the frictional force F_τ, Bull et al. [170] proposed the following equation:

$$F_\tau = \frac{A}{\nu_c}\sqrt{\frac{2E_c\omega}{t}} \tag{4}$$

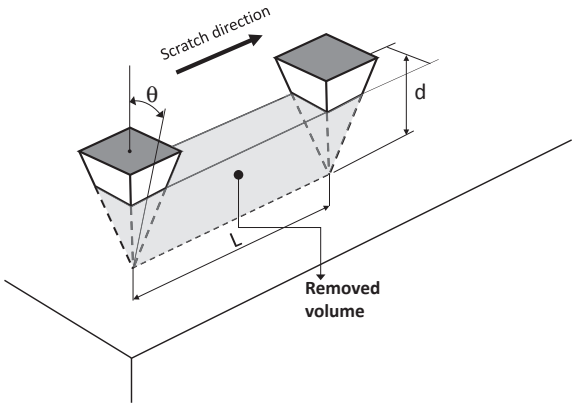

Fig. 13. Schematic of the abrasive wear by a pyramidal indenter.

where A is the cross-sectional area of the wear groove and ν_c is the Poisson's ratio of the coating material. This relationship can be expressed in terms of the normal critical load F_N for coating detachment and COF μ at this load ($F_\tau = \mu F_N$) as follows:

$$F_N = \frac{A}{\mu\nu_c}\sqrt{\frac{2E_c\omega}{t}} \tag{5}$$

6.1.2. Scratch test: Wear rate measurement

Scratch test, in which a diamond stylus ploughs the surface of a material softer than the indenter, can be simplified by a contact model in which the abrasive has a conical shape with a semi-angle θ and the indentation depth of the abrasive is d (Fig. 13). Based on this assumption model, the possible removed volume V, which is ploughed by harder asperities after sliding a distance of L, can be presented by

$$V = d^2\hat{A}\cdot\tan\theta\hat{A}\cdot L \tag{6}$$

Because the normal contact pressure under plastic contact can be speculated to be equal to the hardness H of the wearing material, the bearing contact area can be expressed as

$$2\cdot(d\cdot\tan\theta)^2 = \frac{F_N}{H} \tag{7}$$

By substituting Eq. (7) into Eq. (6), V under F_N and after L can be obtained as follows:

$$V = \frac{1}{2\hat{A}\cdot\tan\theta}\frac{F_N\hat{A}\cdot L}{H} \tag{8}$$

However, as mentioned above, wear depends on not only the geometric considerations of the indenter or the properties of the scratched material but also numerous other factors. To accommodate all these factors, the abrasive wear coefficient K_{ab} is introduced into Eq. (8) as a modifier, and V is described by

$$V = K_{ab}\frac{F_N\cdot L}{H} \tag{9}$$

K_{ab} represents the severity of the scratch process and quantifies the wear rate by scratches.

Eq. (9) provides the removed volume, V, for the case of ideally plastic abrasive grooving during micro-cutting and ploughing (Fig. 11). Each mechanism contributes to the total displaced volume during the scratch test. As reported by Stroud and Wilman [171], during the abrasion of metals, only a proportion of the volume of a wear groove produced by a single scratch is removed as wear debris. The remaining volume of the wear groove is plastically displaced to the edges of the groove. The ratio of the volume of material removed as wear debris to the volume of the wear groove can be described by the fraction f_{ab}, which is defined as

$$f_{ab} = \frac{A_V - (A_1 + A_2)}{A_V} \tag{10}$$

where A_V is the area of the cross-section of the residual wear groove, and $(A_1 + A_2)$ represents the areas of the material accumulated at the groove edges by plastic deformation (Fig. 14). According to Eq. (10), ideal ploughing results in $f_{ab} = 0$, and ideal micro-cutting leads to $f_{ab} = 1$. Generally, f_{ab} ranges from 0.15 to 1.0 [172]. Using f_{ab}, the contribution of both mechanisms, ploughing and cutting, to the wear caused by scratching can be roughly differentiated.

6.1.3. Scratch test: Applications in cold-sprayed coatings

6.1.3.1. Cold-sprayed Al alloy coatings. Pitchuka et al. [173] studied the scratch-induced deformation behaviours of high-pressure cold-sprayed Al amorphous/nanocrystalline alloy coatings at multiple load scales. Micro-scratch tests were conducted at several loads (1000–4000 μN) under constant and ramp-loading conditions. A scratch length of 10 μm and a velocity of 0.33 μm/s were used

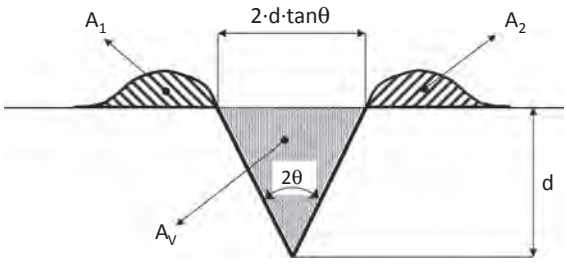

Fig. 14. Cross section of the residual wear groove. The parameters mentioned in Eq. (10) are indicated.

for all the tests. Scratch tests were conducted using a conospherical diamond indenter with a tip radius of 1 μm. These scratches covered two splats in length and a single splat in depth. Macro/high load scratch tests were performed under the following ramp loading conditions: load: 0–5 N; length: 2 mm; and velocity: 8.33 μm/s. In the macro-scratch tests, several splats were affected. In this study, gas-atomised Al amorphous/nanocrystalline alloy spherical powder was deposited on an Al-6061 substrate by CS. The coating thickness was increased to 250 μm. Cold-sprayed Al amorphous/nanocrystalline alloy coatings were thermally annealed at 300 °C for 1 h in a vacuum tube furnace. Then, the performances of the as-sprayed (AS) and heat-treated (HT) Al amorphous/nanocrystalline alloy coatings were analysed. Fig. 15 shows the COF of the AS and HT cold-sprayed Al amorphous coatings after the nanoscratch tests. The COF was slightly lower under the ramp load as compared to that under the constant load. They justified this point by gradually increasing the load along the scratch length. Higher COF values were achieved for the HT coating under all test conditions than those for the AS coating. This may be partially because of the dense structure of the HT coating, which in turn increases the surface shear strength and the COF. Additionally, the COF increased with an increase in the scratch load.

They also examined residual scratch grooves to determine the wear mechanisms. They reported that the dominant material removal mechanism was ploughing in the case of the HT coating, and cutting and chipping in the case of the AS coating. Fig. 16 depicts the representative SEM images showing the deformation and material removal mechanisms of AS (Fig. 16a) and HT (Fig. 16b) cold-sprayed Al amorphous alloy coatings after scratching under constant load conditions [173]. In this figure, the dominant removal mechanisms are presented for each coating.

A tribological study was conducted to estimate the relative wear rates of the AS and HT coatings. These rates were evaluated using Eq. (9). K_{ab} was calculated to be 0.12 and 0.032 for the AS and HT coatings, respectively, under constant load conditions. K_{ab} of the HT coating was ~ 4 times lower than that of the AS coating, indicating higher wear resistance of the HT coating. Higher wear resistance of the HT coating in the microscratch tests was attributed to the densification and formation of hard intermetallic phases, which changed the deformation mechanism to a more ductile mechanism as compared to chipping and cutting in the case of the AS coating. For the macroscratch tests, a normal load of 5 N and a scratch length of 2 mm were selected. Consequently, the load and scratch length were three and two orders of magnitude higher than the corresponding values for the microscratch tests. COF was measured by averaging the COF values determined along the scratch length. The average COF values of 0.28 ± 0.01 and 0.37 ± 0.01 were acquired for the AS and HT coatings, respectively. The values and trend of the COF were relatively similar to those observed during the microscratch tests. The COF value of the HT coating was augmented by its dense structure, which enhanced the surface shear strength and ploughing action during scratching. Residual wear grooves were observed by SEM to identify the wear mechanisms. The degree of deformation was higher during the macroscratch tests as compared to that during the microscratch tests due to the difference in the load scales. The residual grooves were characterised by shear bands at the scratch edges. The presence of shear bands indicated that the deformation was dominated by ductile behaviour.

Chen et al. [174] programmed nanoindentation and nanoscratch tests on cold-sprayed Al composite coatings reinforced with and without C nanotubes (CNTs). Using He as a propellant gas, up to 500 μm thick Al composite coatings were sprayed on AA6061 Al

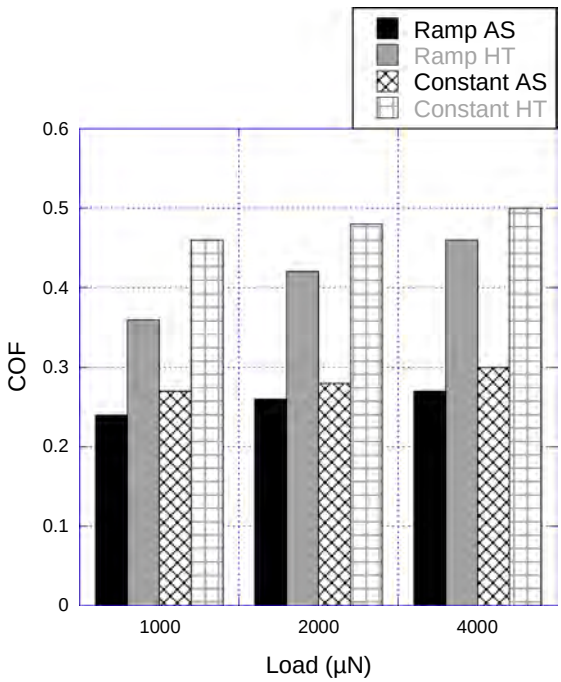

Fig. 15. Coefficients of friction of the as-sprayed (AS) and heat-treated (HT) cold-sprayed Al amorphous coatings after nanoscratch tests. Reproduced from [173].

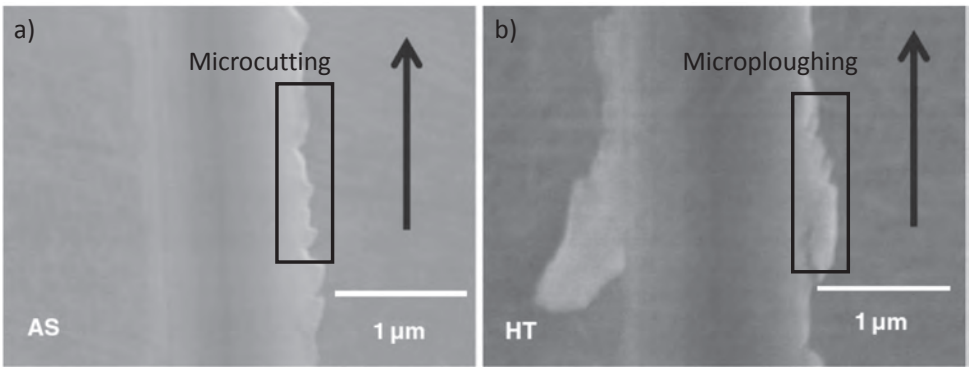

Fig. 16. Representative SEM images showing deformation and material removal mechanisms of (a) AS and (b) HT cold-sprayed Al amorphous alloy coatings after scratching under constant load conditions. Reproduced from [173].

substrates with overall CNT contents of 0, 0.5, and 1.0 wt%. Nanoscratch tests were performed using Hysitron Triboindenter (Hysitron, Minneapolis, USA) with a diamond Berkovich indenter tip having a radius of 100 nm under a constant force of 1000 µN at a scratching speed of 0.33 µm/s and a total scratch length of 10 µm. During the scratch tests, the COF was calculated as the ratio of the instantaneous lateral force and normal force. Residual grooves were investigated by scanning probe microscopy (SPM). SPM images were utilised to determine the volume of the material displaced during scratching. This volume was estimated via the following equation:

$$V = \int_{-l/2}^{l/2} \frac{1}{2} [\tan\varphi + \tan(\theta - \varphi)]h^2 dx \tag{11}$$

where l is the scratch length, h is the depth of the groove at the scratch distance x, θ is the angle between the faces of the scratch groove, and ϕ is the angle between one of the faces and the normal direction. The angular parameters stated in Eq. (11) are depicted in Fig. 17.

The higher the CNT content, the lower the residual volume of the scratch groove. The wear resistance of pure Al improved by 40% with the addition of 1 wt% CNTs. The lateral force and COF for the three cold-sprayed coatings during the nanoscratch tests did not significantly vary. The average COF values were found to be 0.17 ± 0.01, 0.19 ± 0.01, and 0.18 ± 0.02 for Al, Al–0.5CNT, and Al–1CNT coatings, respectively. The small effect of the CNT content on the COF was validated by the fact that the CNTs were intact, and the graphitic lubrication mechanism was not operational unless there was substantial damage to the CNTs to generate graphite-like debris. SPM images of the residual grooves revealed that the wear was dominated by ploughing and micro-cutting. However, the addition of CNTs increased the resistance of pure Al to micro-cutting probably because CNTs improved the hardness and strength of pure Al.

6.1.3.2. Cold-sprayed Ti alloy coatings. Sirvent et al. [175] conducted local scratch tests on Ti6Al4V coatings (Ti6Al4V) deposited by CS using an upstream system. Ti6Al4V were separately cold-sprayed on the same bulk alloy at gas temperatures of 800 °C (Ti6Al4V-800 °C) and 1100 °C (Ti6Al4V-1100 °C) to improve the performances of Ti6Al4V. Ti6Al4V was sprayed using an HPCS system (Impact

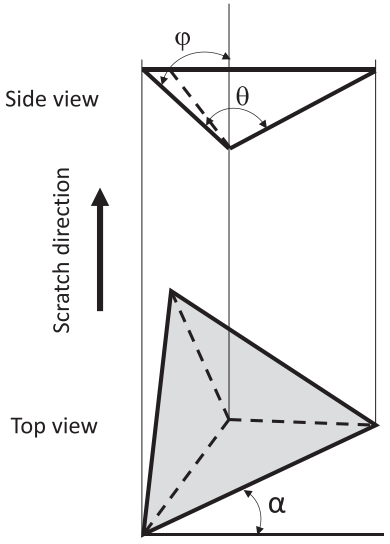

Fig. 17. Top and side views of Berkovich indenter with the angular parameters stated in Eq. (11).

Innovations 5/11, Impact Innovations, Ampfing, Germany) equipped with a water-cooled SiC nozzle. Herein, two sets of gas temperature and pressure were employed: 800 °C and 4 MPa and 1100 °C and 5 MPa, respectively. Several Ti6Al4V-1100 °C were heat-treated (Ti6Al4V-1100 °C-HT) after spraying to enhance their adhesion and reduce their porosity. Heat treatment was followed by precipitation. Fig. 18 shows representative SEM images of the cross-sections of coatings. From the SEM investigation of the cross-sections of the coatings, a maximum porosity of approximately 17% was obtained for Ti6Al4V-800 °C, which reduced up to 2.9% for Ti6Al4V-1100 °C and 1.7% for Ti6Al4V-1100 °C-HT. Local scratch tests were performed using a Berkovich diamond indenter with a tip radius of 20 nm and the largest edge as the leading border. Transverse and longitudinal depth profiles of the residual groove were measured to evaluate the volume of the residual groove per unit of scratch distance, V, by the following equation:

$$V = \frac{1}{L}\int_0^L \tan\theta\hat{A} \cdot h^2 dx \tag{12}$$

where h is the real residual depth, which depends on the scratch distance x; L is the scratch length, fixed at 400 μm; and θ is the semi-angle between the faces of the scratch groove, measured from the transverse residual profile considering the transverse area as a triangle. Eq. (12) is a simplified alternative to Eq. (11).

Scratch tests were conducted using four normal loads (Fn): 10, 50, 100, and 150 mN. In addition, three scratch velocities were employed: 10, 20, and 40 μm/s. Dimensionless wear coefficient for the scratch tests, K_S, was calculated as

$$K_S = \frac{V \cdot H}{F_n} \tag{13}$$

where H is the hardness of the coatings and the substrate, which was previously measured by nanoindentation. Equation (13) is very similar to Eq. (9). Ks values for all the tested materials were obtained from the slope of the V vs. Fn/H curve using Eq. (13). K_{ab} values of 3.09 ± 0.40, 9.69 ± 1.30, 3.19 ± 0.54, and 4.04 ± 0.50 were achieved for the substrate, Ti6Al4V-800 °C, Ti6Al4V-1100 °C, and Ti6Al4V-1100 °C-HT, respectively. Upon comparing the Ks values of the different materials, Ti6Al4V-800 °C was found to exhibit the lowest wear resistance. The substrate demonstrated the lowest wear rate. Ti6Al4V-1100 °C presented a K_S value similar to that of the substrate. Finally, the wear rate of Ti6Al4V-1100 °C-HT was slightly higher than that of the substrate. SEM images of the residual wear grooves produced during the scratch test at 100 mN are shown in Fig. 19.

Grooves on the Ti6Al4V substrate (Fig. 19a) were characterised by the simultaneous action of ploughing and micro-cutting mechanisms. The contributions of both mechanisms to wear seemed similar. The grooves of Ti6Al4V-800 °C were characterised by an additional wear mechanism consisting of spalling (Fig. 19b). This mechanism mainly occurred at the intersplat boundaries. This additional wear mechanism may explain the higher value of K_{ab} obtained for Ti6Al4V-800 °C. The grooves of Ti6Al4V-1100 °C were primarily characterised by ploughing, with no significant contribution of micro-cutting to wear (Fig. 19c). This may explain why Ti6Al4V-1100 °C showed the lowest K_{ab} among those of the three coatings. The absence of spalling could be an indication of the high strength of the interface between splats. It can be concluded that the spraying parameters used to manufacture these coatings resulted in a strong bonding between the splats, and therefore, coatings with high cohesion were acquired. Both the micro-cutting and ploughing mechanisms were discovered in the residual grooves of Ti6Al4V-1100 °C-HT (Fig. 19d). Thus, there is a clear and direct relationship between the wear mechanisms and K_{ab}. Therefore, K_{ab} is a measure of the severity of wear that depends on the wear mechanisms activated during the scratch test.

6.2. *Wear behaviour: Dry sliding tests.*

When two surfaces are sufficiently close, contact occurs between multiple asperities that constitute the surface roughness of the two surfaces in contact. Accordingly, the true contact area is equal to the sum of the individual asperity contact areas. This area is closely proportional to F_N. Because of this contact, the deformation of the asperities is speculated to be plastic. Therefore, this contact area may be hypothesised to be inversely proportional to the hardness of the material. If only a proportion of all asperity contacts leads to wear particles and these asperities are considered to be a hemisphere, the following relationship between the volume worn per unit sliding distance, Q, to F_N and the hardness of the softer surface, H, can be supposed:

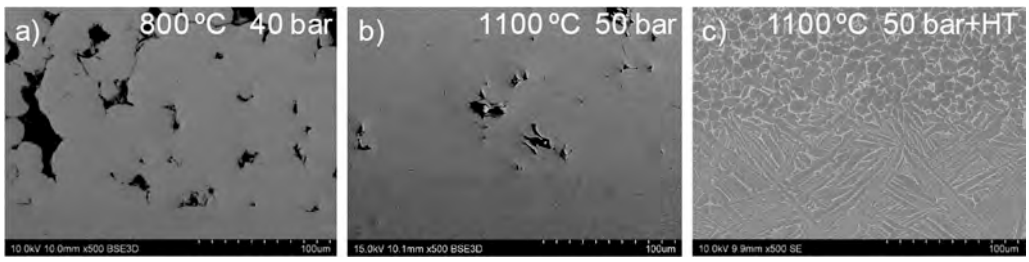

Fig. 18. SEM images showing the cold-sprayed coatings and the coating-substrate interfaces subjected to the following conditions: (a) 800 °C, 4 MPa; (b) 1100 °C, 5 MPa; (c) heat treated coating. Reproduced from [175].

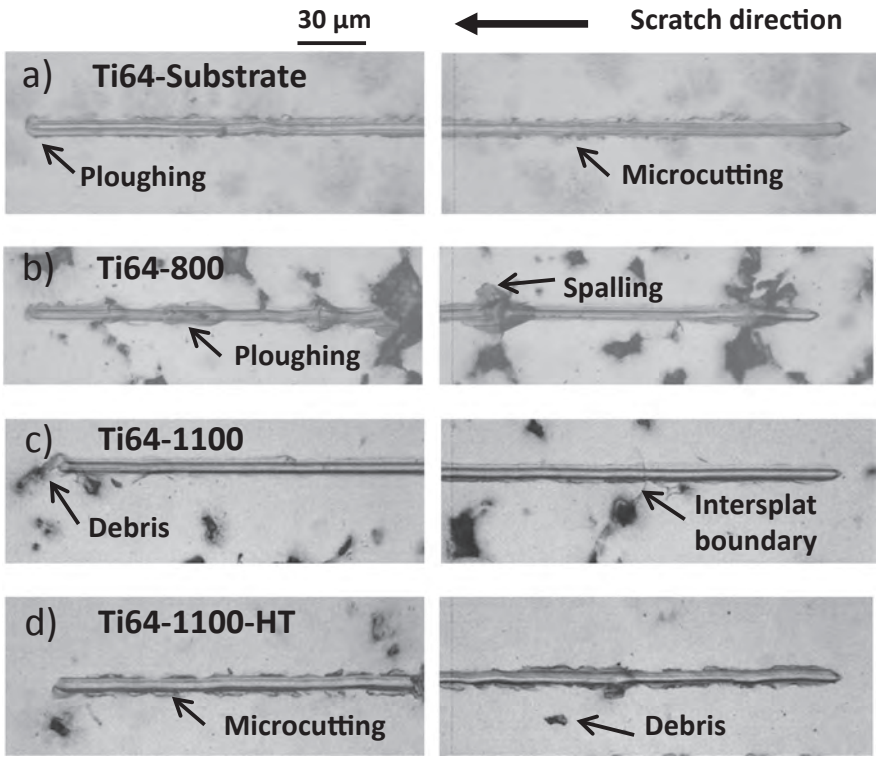

Fig. 19. SEM images of the residual scratch grooves on (a) the substrate; (b) Ti6Al4V sprayed at 800 °C; (c) Ti6Al4V sprayed at 1100 °C; (d) Ti6Al4V sprayed at 1100 °C followed by heat treatment.

$$Q = \frac{V}{L} = K\frac{F_N}{H} \tag{14}$$

where V is the total worn volume, L is the sliding distance, and K is a dimensionless constant, usually known as the wear coefficient. K provides a valuable means of comparing the severity of wear processes in different systems. Equation (14) is called the Archard wear equation [176,177]. The value of K depends on how the contact between the two surfaces, counterbody and coating is established and consequently on the mechanisms by which wear occurs. During the relative slip between the two surfaces, local plasticity is induced between the asperities of both contact surfaces. The microstructure of the metal close to the surface is modified such that the coating grains or splats are often refined to agglomerates composed of fine grains of nanocrystalline structures [178]. This layer is addressed by different names: 'tribofilm', 'tribolayer', and most commonly 'mechanically modified layer' or 'mechanically mixed layer' (MML). Morphology, composition, and properties of this layer have a substantial influence on wear. In sliding contact, wear can occur because of adhesion, surface fatigue, tribochemical reactions, and/or abrasion [176]. Many factors affect the dominant wear mechanism. Among them, the roughness of the contact surfaces, metallurgical and mechanical pairing properties, tribochemical pairing properties, and experimental test conditions have a considerable influence on the generation and characteristics of MML.

Cold spray deposition provides an opportunity to repair components that have been damaged during their service life because it can produce thick coatings with limited residual stresses. Moreover, it offers an opportunity to repair the components by spraying coatings with higher resistances to damage than that of the substrate. Numerous strategies, including optimising the spraying process, heat treatments, and addition of hard metals or ceramics, solid lubricants, or some form of composites, have been proposed to increase the wear resistances of cold-sprayed coatings [15,179,180]. In tribological systems that operate under sliding conditions, the effect of the interfacial contact layer on wear should be considered. If interfacial shear strength is low, the contact area and friction increase. Thus, if the contact area is reduced, low friction would be expected. The contact area is commonly reduced using harder coatings. However, the interfacial shear strength may increase due to the hard contact, and therefore, the friction can increase. Another way to reduce the contact area is using coatings with lubricating properties. This decreases the shear strength. Nevertheless, depending on the level of solid lubricant added to the coating, the mechanical properties of the coating may decrease, increasing the contact area. An alternative way is using a combination of both the abovementioned strategies, generating a contact interface that has lubricating properties and is reinforced with ceramic or oxide phases, whose hardness is generally higher than those of metals. The presence of hard particles is associated with lower wear rates and friction as compared to those of the unreinforced matrix material. Because of this, CS deposition of ductile metals (Al alloys) having low shear strengths and reinforced with hard particles (Al_2O_3 or SiC) has attracted attention [181–186].

Hereinafter, the study of the wear resistances of cold-sprayed coatings by dry sliding has been discussed.

6.2.1. Continuous dry sliding test: Cold-sprayed coatings

6.2.1.1. Cold-sprayed Al alloy coatings. Al and its alloys demonstrate poor tribological behaviours and low wear resistances, which limit their use in many applications [187]. An alternative way to maintain the corrosion resistance, low density, and high thermal conductivity of Al and its alloys is to enhance their tribological responses using Al matrix composite (Al-MMC) materials, in which secondary hard phases, generally based on SiC, WC, or Al_2O_3, provide mechanical reinforcement to the Al matrix [188]. The Al-MMC materials developed to date show corrosion resistance comparable to that of pure Al and wear rates lower than that of pure Al [186,189–191]. The hard particles plastically constrain the Al matrix, which improves the high-temperature, mechanical, and wear resistance properties and decreases the friction of the Al matrix as compared to those of the unreinforced matrix material [192,188,193]. Therefore, Al-MMCs are widely used in the production of pistons, connecting rods, engine cylinders, discs, and drum brakes as wear resistance plays a crucial role in the functioning of these components [188,194–197]. However, the wear resistance of metal matrix composites also depends on various microstructural characteristics such as particle size, volume fraction, distribution, and shape of the reinforcement material [164,198–201]. For example, in the case of Al-MMC materials, wear rates decrease with an increase in the content of hard particles [202].

Cruz et al. [203] evaluated the wear resistances during service for high-pressure cold-sprayed Al-2024, Al-F357, and Al-C355 coatings deposited on corresponding bulk alloys under continuous and oscillating conditions using a pin-on-disk configuration. The behaviours of the substrates were also investigated to compare the performances of the coatings with those of the original bulk alloys. The influence of a hard superficial layer on the wear behaviours of the cold-sprayed coatings and substrates was tested before and after anodisation. N_2 was employed as the process gas for all depositions. The coatings were sprayed on the corresponding Al bulk alloys to simulate the operating conditions of the aeronautical component. Table 1 presents the various deposition conditions. Microstructures of the sprayed coatings improved when the temperature and/or pressure were increased by reducing the porosity and delamination of the substrate. However, the generation of a denser coating does not necessarily result in better wear behaviour.

Upon comparing the wear behaviours of C355 and C355+, the COF values of C355 and C355+ were found to be similar (approximately 0.1 and 0.9) under oscillating and sliding conditions, respectively. A similar result was obtained for the as-sprayed coating (2024), where there were no significant differences between the COF values of 2024 and 2024 under an enhanced spraying condition (2024+). The wear rate of 2024 decreased with an increase in the spray temperature and pressure. In contrast, the wear rate of C355 did not show this tendency during the sliding wear tests. Heat treatment did not have a considerable beneficial effect on the tribological behaviours of coatings. The COF values of C355+ and C355+HT did not show a significant difference. Under the sliding condition, wear rates decreased when the coatings were subjected to post-heat treatment. However, under the oscillating condition, the effect of heat treatment on the wear rate was negligible. Based on the variation tendencies of the COF and wear rates, it was deduced that plastic deformation and the generation of MMLs play a key role in the wear of these coatings. Anodisation was conducted to analyse the effect of a continuous superficial layer with high hardness on the wear behaviours of coatings. According to the results reported in this study, it was concluded that this layer did not significantly improve the wear resistances of the investigated coatings. This conclusion supports the idea that the incorporation of hard particles during spraying may be a more efficient approach to increase the wear resistances of coatings.

Recently, CS has been utilised for the deposition of Al-MMC coatings, in which hard phases can be incorporated by mixing them with feedstock powders [186,204,205]. Spencer et al. [204] sprayed pure Al and 6061 Al alloy-based Al_2O_3 particle-reinforced composite coatings on AZ91E Mg alloy substrates via CS using He as the propellant gas. Spherical commercial-purity Al and Al 6061 alloy powders with average particle sizes of 15 and 22 μm, respectively, were employed. α-Al_2O_3 powder with an average particle size of 20 μm was used as a reinforcement, which was mixed with Al powder to achieve mixtures comprising 25, 50, and 75 vol% Al_2O_3. He was used as the carrier gas under a driving pressure of 620 kPa. Before accelerating the powder/gas mixture through the nozzle, the temperature of this mixture was maintained at 125 °C. Mass flow rate of the powder mixture injected into the gas stream was 15 g min^{-1}. The standoff distance of the nozzle from the substrate was 12 mm, and the traverse speed was 50 mm min^{-1}. Corrosion and wear of cold-sprayed pure Al coatings were examined under both the as-sprayed conditions and after post-heat treatment at 400 °C for 2 h under an Ar atmosphere. The Al 6061 coatings were only tested under the as-sprayed condition. Dry sliding wear tests of cold-sprayed Al–Al_2O_3 coatings were performed using a unidirectional pin-on-disk tribometer with a 6 mm bearing steel ball and a normal load of 3 N over a wear length of 500 m. They concluded that the presence of Al_2O_3 particles led to a stable COF and

Table 1
Spraying parameters of cold sprayed coating reported by Cruz et al. From [203].

Coating	Gas temperature (°C)	Gas pressure (MPa)	Post-treatment	Code
Al-C355	350	4		C355
	500	6		C355+
	500	6	4 h at 150 °C	C355 + HT
	500	6	4 h at 150 °C + anodised	C355 + HT-A
Al-2024	350	4		2024
	350	6		2024+
	350	4	Anodised	2024 A
	350	6	Anodised	2024 + A
Al-F357	450	5.7		357
	450	5.7	Anodised	357 A

substantially reduced the wear rates as compared to those of the unreinforced pure Al and AA6061 coatings. The cold-sprayed pure Al coating demonstrated a residual groove with a morphology typical of adhesive wear. Wear tracks of Al–25% Al_2O_3 and Al–50% Al_2O_3 coatings showed signs of smearing and adhesive wear similar to those in the case of the pure Al coatings; however, some evidence of abrasive wear and oxidation of the wear debris were also noticed. The worn surface of the Al–75% Al_2O_3 coating was characterised by abrasive wear. Therefore, the wear behaviour of this coating changed from adhesive to abrasive with an increase in the Al_2O_3 addition content. This transition was reflected by a significant reduction in the wear rate of the coating. This change in the wear behaviour was accompanied by a high and more stable COF. Once the wear behaviour became fully abrasive, the wear rate was reduced by several orders of magnitude. The high content of reinforcing particles limited the plastic deformation ability of the coating in contact with the counterbody, favouring the abrasive wear mechanism. The shear strength probably increased owing to the high content of Al_2O_3 particles, decreasing the contact area and consequently the removed volume.

Shockley et al. [206,207,149] examined the effects of the concentration and morphology of Al_2O_3 particles on the friction and wear mechanism of low-pressure cold-sprayed Al–Al_2O_3 coatings. Feedstock powders for CS were prepared by admixing commercially available spherical Al powders with different contents of Al_2O_3 powder. For CS, the inlet N_2 gas temperature and pressure were fixed at 500 °C and 0.62 MPa, respectively. The gun was maintained at a constant standoff distance of 1 cm and moved across the substrate surface at a transverse speed of 2 mm/s. The powder was fed at a rate of 8–12 g/min using an external powder feeder with N_2 carrier gas at a flow rate of 3 L/min. The coatings were deposited on mild steel substrates with a thickness of 500–600 μm [186,206]. A reciprocating ball-on-flat tribometer was employed to perform dry sliding wear tests. All wear tests were conducted at a sliding speed of 3 mm/s and a track length of 10 mm. Hemispheres (diameter: 6.35 mm) of monocrystalline α-Al_2O_3 (sapphire) were used as the counterface material. Fig. 20 shows the secondary electron (SE) images of the cross-section of the etched unworn microstructures of as-sprayed Al (Fig. 20a) and Al–22% Al_2O_3 (Fig. 20b) coatings. Particle boundaries (white arrows in Fig. 20a) can be observed in the etched microstructures. Moreover, Al_2O_3 particles are embedded in the Al matrix (white arrows in Fig. 20b).

During the wear tests, the COF was continuously recorded. The COF of the cold-sprayed pure Al coating fluctuated between 0.6 and 1.3 with many spikes and temporary shifts. However, a COF between 0.5 and 0.7, implying a more stable friction behaviour, was observed for the cold-sprayed Al–Al_2O_3 coating. Similar stabilisation of friction because of Al_2O_3 during the dry sliding of Al and Al–Al_2O_3 coatings has also been reported in other studies [204,208].

Wear tests of the cold-sprayed pure Al coating indicated extensive ploughing, and the removed material accumulated ahead of the slider until a critical length was achieved. Then, this material detached from the contact and remained on the wear track. Subsequently, a new prow was immediately generated. As this process continued, some ejected prow material was left at the ends of the wear track as wear flow. The formation and detachment of several prows resulted in a permanent MML. Wear was characterised by a large plastic flow of the MML and frequent detachment of the material from the contact. Furthermore, at the points where the COF underwent large shifts from one steady-state value to another, the transfer film exhibited corresponding detachments of large patches of material. The wear track is a characteristic of adhesive wear [204]. Layered structures of adhered material were noticed, providing a highly inhomogeneous wear track (Fig. 21a). The wear debris exhibited a flake morphology.

In contrast, the plastic flow in the case of the cold-sprayed Al–Al_2O_3 coating was limited. Consequently, the MML remained stable throughout the wear test. Additionally, the extension of MML was restricted. Neither ejection flows nor jumps were observed in the COF. Therefore, the stability of the MML and COF was promoted by the introduction of Al_2O_3 particles. The wear track demonstrated a lack of prominent prows. The MML was relatively smooth and coherent with the extensive surface texture in the sliding direction, indicative of micro-ploughing (Fig. 21b). The MML consisted of fine-grained Al with fractured Al_2O_3 particles. Nanoindentation tests revealed the production of a uniform and hardened MML on Al–Al_2O_3 coatings. This hardening increased the resistance of the coatings to adhesion. Shockley et al. [206,149] concluded that generally, with an increase in the Al_2O_3 content of the coating, the wear resistance increases and the wear behaviour of the Al–Al_2O_3 composite coating gradually changes from adhesive to abrasive. Furthermore, they reported that Al_2O_3 particles with spherical morphologies provided higher wear resistance to the coating than that endowed by Al_2O_3 particles with angular morphologies with a similar content in the coating.

Wu et al. [209] deposited coatings comprising different proportions of α-Al_2O_3 and pure Al on AZ91D Mg alloy substrates by CS. Commercially pure spherical Al particles (99.5 wt%), produced by GA, were blended with irregular α-Al_2O_3 particles with an average

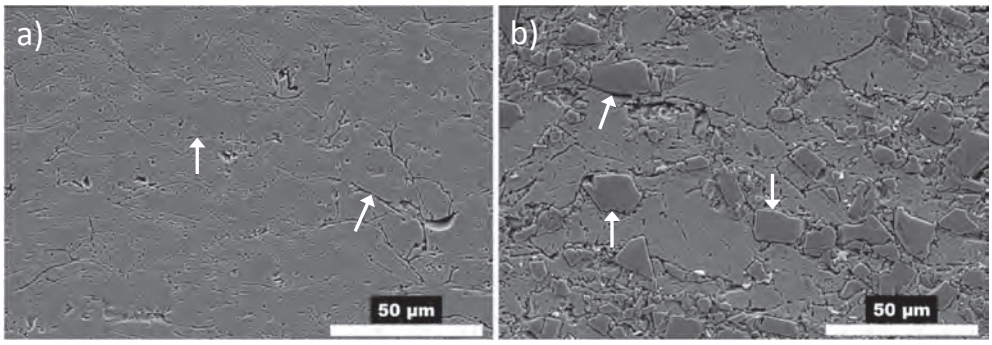

Fig. 20. Secondary electron (SE) images of the cross-section of the etched unworn microstructures 250 μm below the surface: (a) as-sprayed Al coating and (b) Al-22% Al_2O_3. Reproduced from [207].

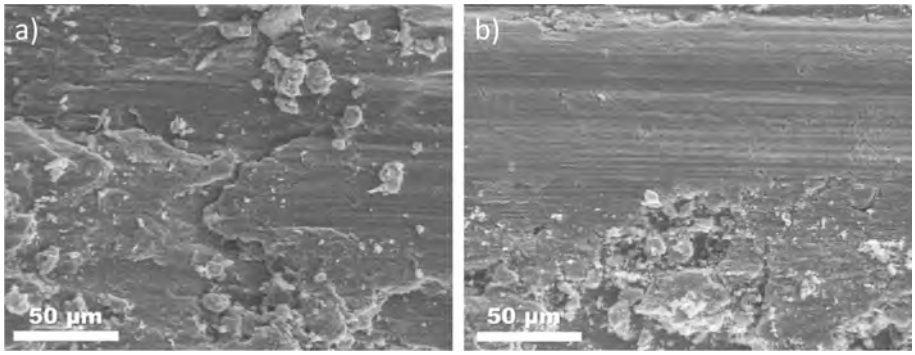

Fig. 21. Representative wear tracks of (a) cold-sprayed pure Al coating and (b) cold-sprayed Al-20% Al_2O_3. Reproduced from [209].

size of 25 μm. The proportions of α-Al_2O_3 in the feedstock were 25, 50, and 75 wt%. For CS, the gas temperature and pressure were set at 230 °C and 1.6 MPa, respectively. Friction and wear properties of the coatings were evaluated by a ball-on-disk wear tester. The counterbody was a GCr15 ball with a diameter of 6.35 mm. The sliding speed was maintained at 30 r/min during the entire test, and the load between the pin and the disk was 10 N.

Contrary to the conclusions reported by Shockley et al. [206,149], Wu et al. [209] observed that the wear mechanisms were strongly dependent on the α-Al_2O_3 content. The wear track of pure Al demonstrated a typical adhesive wear. The wear track generated on the coating with 25 wt% α-Al_2O_3 showed features similar to those in the case of pure Al. Consequently, the main wear mechanism was determined to be adhesive wear. For the coating containing 50 wt% α-Al_2O_3, the wear mechanism was identified as a combination of adhesive and abrasive wear mechanisms. Wear behaviour of the coating with 50 wt% α-Al_2O_3 completely changed to abrasive wear. Consequently, with an increase in the content of α-Al_2O_3 particles, the wear behaviour of the coating transformed from adhesive wear to abrasive wear. This transition was also indicated by the corresponding wear rates. However, the coating with 75 wt% α-Al_2O_3 showed a lower wear rate than that of pure Al. The coatings with lower contents of α-Al_2O_3 exhibited higher wear rates than that of pure Al owing to the combined effect of adhesive and abrasive wear mechanisms. This result shows some discrepancy with that reported by Shockley et al. This discrepancy indicates that different values of the spraying parameters and different conditions of wear tests may lead to slightly different results. Therefore, this topic is still debatable.

6.2.1.2. Cold-sprayed Ti alloy coatings. Ti6Al4V exhibits low resistance to abrasive wear, which limits its application in components where wear resistance is a crucial requirement. Nevertheless, several studies have reported that cold-sprayed Ti6Al4V coatings demonstrate higher wear resistances than those of commercial Ti6Al4V bulk materials [210–212]. Khun et al. [210,211] investigated the hardnesses and wear and corrosion resistances of Ti6Al4V coatings deposited by CS. Commercial Ti6Al4V powder with a spherical shape and a size of 15–45 μm was deposited on a commercial Ti6Al4V substrate using HPCS. The working gas, gas temperature and pressure, standoff distance, and nozzle speed used for CS deposition were N_2, 1000 °C and 5 MPa, 30 mm, and 300 mm/s, respectively. A ball-on-disk micro-tribological test was performed according to the DIN 50324 [213] and ASTM G99 [214] standards to evaluate the tribological properties of the coatings. A 100Cr6 steel ball with a diameter of 6 mm was fixed on the surface rotating in a circular path of 1 mm radius for 30,000 laps at a sliding speed of 3 cm/s under a normal load of 1 N. The COF and specific wear rate of 0.52 ± 0.01 and 92.9 ± 16.4 × 10^{-14} m^3/(Nm), respectively, were acquired for the Ti6Al4V coating. The COF and specific wear rate of the commercial Ti6Al4V substrate tested against the steel ball under the same conditions were 0.55 ± 0.01 and 93.9 × 10^{-14} m^3/(Nm), respectively. Abrasive grooves were observed on all the wear tracks of the Ti6Al4V coating because of the significant abrasive wear

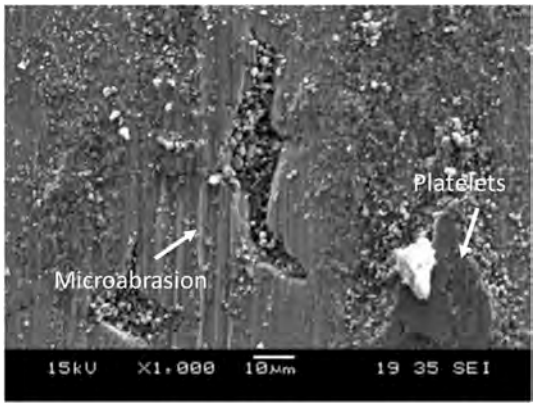

Fig. 22. Morphology of the wear groove of the Ti6Al4V coating. Reproduced from [211].

caused by the repeated sliding of the steel ball. Micro-abrasive wear was noticed during the analysis of the residual grooves of Ti6Al4V coatings. Additionally, platelets were observed on the wear tracks of the Ti6Al4V coatings (Fig. 22). Repeated sliding of the steel ball may initiate cracks, which, based on their extent, may lead to the detachment of platelets by fatigue.

Sirvent et al. [212] examined the wear resistances of Ti6Al4V coatings deposited on the substrates of the same Ti alloy by HPCS. Unidirectional sliding wear tests were conducted in a pin-on-disc configuration, where the pin was the coating and the disc was a bearing steel (100Cr6) counterbody. A normal pressure of 30 MPa and a sliding speed of 0.26 m/s were employed. Wear tests were performed at two different temperatures: RT and 450 °C. Moreover, two different cold-sprayed Ti6Al4V coatings were deposited. For the first batch of coatings, a gas temperature and pressure of 800 °C and 4 MPa (Ti64-800), respectively, were used. For the second batch of coatings, a gas temperature and pressure of 1100 °C and 5 MPa (Ti64-1100), respectively, were selected. COF values of ~0.3 and ~ 0.45 were obtained for the tests conducted at RT and 450 °C, respectively. These values were retained in the cases of the bulk alloy and both coatings. Therefore, the higher the test temperature, the higher the COF. Additionally, the removed mass of the pin (δm) at RT was substantially higher than that measured at 450 °C for both the bulk material and the coatings.

However, upon comparing the wear rates of the different materials at RT, it was found that the wear resistances of Ti64-800 and Ti64-1100 did not significantly improve as compared to that of the bulk alloy. Nevertheless, a considerable improvement in the wear resistances of coatings was observed at 450 °C.

Fig. 23 depicts representative SEM images of the residual grooves obtained on the substrate (Fig. 23a and d), Ti64-800 (Fig. 23b and e), and Ti64-1100 (Fig. 23c and f) at RT and 450 °C, respectively. The contact between the pin and the disc was characterised by the generation of an MML. The material detached from and adhered to the contact surface was in the form of highly deformed platelets, which indicated adhesion between the pin and the counterbody. Consequently, adhesion mechanism may activate during the wear tests. Nevertheless, the contribution of this mechanism varied depending on the wear test conditions. Higher number of larger platelets were observed on the bulk alloy (Fig. 23a). Moreover, no substantial scratches were noticed. Thus, adhesive wear may be the main wear mechanism. The MML of Ti64-800 (Fig. 23b) exhibited highly deformed platelets and scratches, revealing a combination of adhesion and abrasive wear mechanisms, increasing the wear rate. The MML of Ti64-1100 (Fig. 23c) showed lower amount of transferred material as platelets, implying a lower contribution of the adhesion wear mechanism probably due to the higher shear strength of this coating. However, significant scratches were observed on this coating, indicating a higher contribution of the abrasive wear mechanism. At 450 °C, the number of platelets adhered to the contact surface substantially decreased in the case of the coatings as compared to that in the case of the bulk alloy. Furthermore, fewer scratches were noticed at 450 °C than those at RT, suggesting lower contribution of the abrasive wear mechanism. This may justify the improvement in the wear resistances of the coatings at 450 °C as compared to that of the bulk alloy.

6.2.2. Oscillating dry sliding test: Cold-sprayed coatings.

6.2.2.1. Cold-sprayed Al alloy coatings. Attia et al. [215] compared the friction and fretting wear properties of repaired surfaces using various coating compositions and spraying techniques. Herein, eight types of cold-sprayed coatings deposited on AMS4260 Al substrates were fretted against 440C stainless steel specimens at low and high nominal loads to assess their fretting wear resistances, friction properties, and damping capacities. A flat-on-flat configuration with an amplitude of 20 μm was selected for the fretting tests.

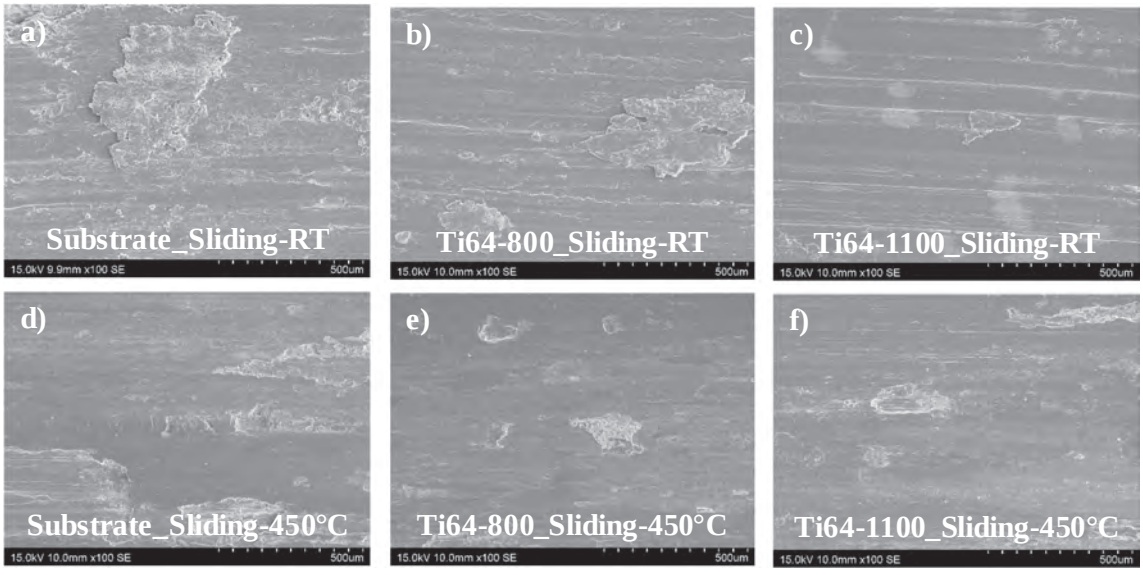

Fig. 23. SE images of the worn surface of the substrate (a and c), the Ti6Al4V-800 coating (b and e) and the Ti6Al4V-1100 coating (c and f) tested under continuous sliding conditions at RT and 450 °C. Reproduced from [212].

The contact pressures for the low and high nominal normal loads were 3.72 and 13.44 MPa, respectively. The frequency of the oscillations of the tests at low nominal normal load varied between 150 and 155 Hz. For the tests conducted at high nominal normal loads, the frequency of vibration was 185 Hz. Fretting wear tests were performed for 50 h. Wear resistance of the coated surface was determined by the specific wear coefficient K (Eq. (14)). They studied the wear behaviours of different cold-sprayed composite coatings: Al + 5% Al_2O_3 and Al–Cr. They concluded that the Al–Cr coating provided the best results. Compared to uncoated Al, this coating showed equivalent wear resistance properties and better friction properties. The addition of Al_2O_3 did not improve the wear behaviour of the coating as compared to that of uncoated Al. Different wear mechanisms were involved in wear. Tribolayers developed by the adhesion and transfer of material between the two surfaces were observed. For the composite coatings with 5% Al_2O_3, the formation of Al oxide promoted wear damage by inducing three-body abrasion, increasing the wear rates when compared with that of the uncoated material.

6.2.2.2. Cold-sprayed Ti alloy coatings. During the oscillating–fretting wear tests of Ti alloys, multiple wear mechanisms, such as adhesive, abrasive, and oxidative wear, can sequentially or simultaneously occur; hence, oscillating wear is not a basic but a complex wear mechanism.

Sirvent et al. [212,216] performed oscillating sliding wear tests to determine the wear resistances of Ti6Al4V coatings deposited on the substrates of the same Ti alloy by HPCS. These tests were conducted at RT and 450 °C using the pin-on-disc configuration. A normal pressure of 30 MPa and a rotation amplitude of 298 μm with a frequency of 40 Hz were selected. The number of cycles was fixed at 1,00,000. The coatings were sprayed using two different sets of gas temperature and pressure: 800 °C and 4 MPa (Ti64-800) and 1100 °C and 5 MPa (Ti64-1100), respectively. Some of the Ti64-1100 coatings were heat-treated (Ti64-1100-HT) after spraying to reduce their porosity and enhance their adhesion. A solution heat treatment was executed at 1000 °C for 1 h in high vacuum ($<10^{-7}$ Torr) at a heating rate of 10 °C/min followed by Ar quenching to RT. Thereafter, precipitation was performed at 537 °C for 4 h at a heating rate of 10 °C/min followed by furnace cooling. The COF values and wear rates are shown in Fig. 24.

COF can be considered indicative of the wear mechanism that is activated during the wear test. As shown in Fig. 24a, the COF values obtained via the wear tests at 450 °C are higher than those acquired at RT. Ti64-1100 exhibits better tribological properties than those of the bulk material. The COF values obtained at 450 °C and RT were similar only for Ti64-1100-HT. Furthermore, Ti64-1100-HT showed a higher COF and simultaneously a lower wear rate (Fig. 24b) than those of the substrate and other coatings, revealing its high wear resistance.

Ti64-1100 (Fig. 25a) demonstrated platelets adhered to the wear track after the oscillating wear test at RT. Sirvent et al. [212,216] discovered adhesion as the main wear mechanism at RT. Nevertheless, during the wear tests at 450 °C, the formation of Ti and Fe oxides was favoured. Platelets combined with microscratches were noticed on the wear track, suggesting a combined effect of two wear mechanisms (adhesion and abrasive) (Fig. 25b), justifying the increase in the wear rate (Fig. 24b). They reported the generation of a continuous and hard layer of Ti oxide on the Ti64-1100-HT surface due to the heat treatment. This layer must have had a substantial effect on the wear resistance of the coating mainly because of its stability at high temperatures. The oxidation of Ti significantly improves its tribological properties. TiO_2 showed a smoother COF profile with less fluctuations and demonstrated a lower value of COF as compared to those of a Ti plate, which exhibited an unstable COF with evident fluctuations. The same behaviour was observed for the cold-sprayed coating. The improvements were also indicated by the limited wear rate of the oxidised coating, which was considerably lower than those of the as-sprayed Ti coating and Ti bulk material. Krishna et al. [217] confirmed this behaviour. They supposed that the improvement in the wear resistance was caused by the high hardness of the oxide layer and its strong adhesion to the underlying material. Dalili et al. [218] verified the role played by the formation of a harder oxide layer in improving the wear resistance of Ti, resulting in a lower COF and negligible weight loss. They hypothesised that the oxide layer prevented extensive plastic deformation of Ti, thereby changing the nature of the contact surface [219–221].

Alidokht et al. [222] investigated the sliding wear behaviour of a Ti–TiC coating deposited by HPCS. Mixtures of mechanically

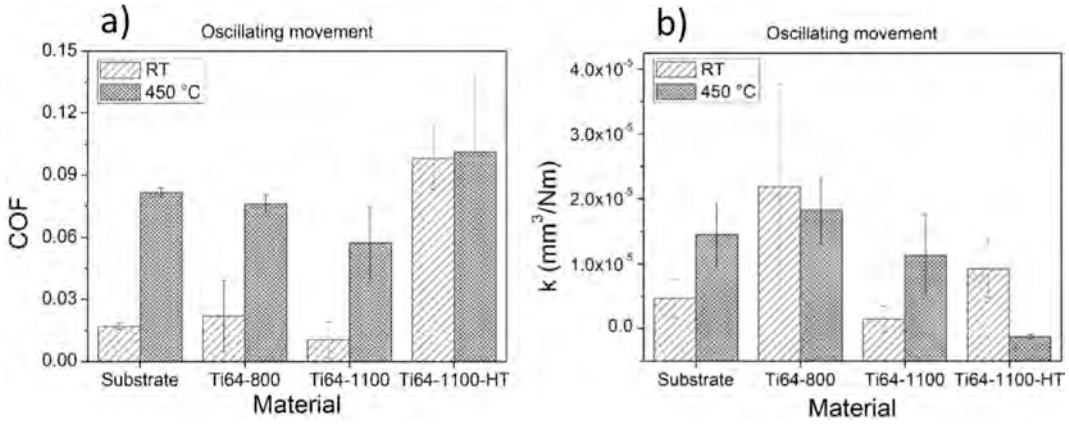

Fig. 24. Coefficients of friction (a) and wear rates (b) of cold-sprayed Ti6Al4V coatings and substrate measured via wear tests. Reproduced from [216].

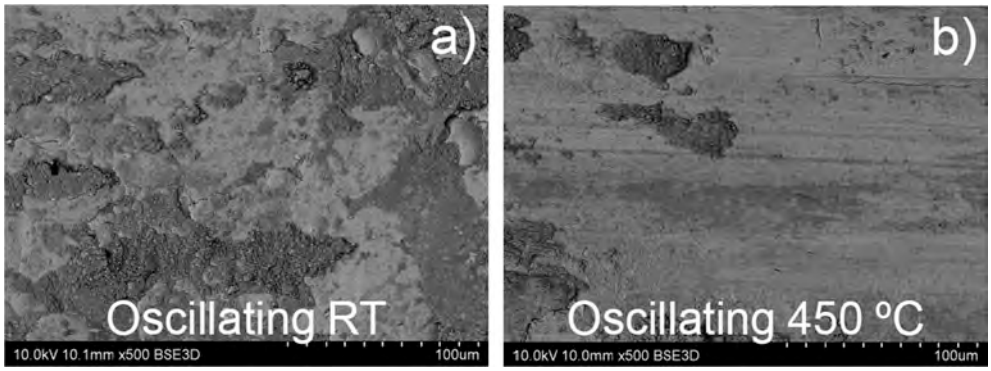

Fig. 25. Backscattered electron images from the worn surfaces of the cold-sprayed Ti6Al4V coating at 1100 °C and 5 MPa after sliding and oscillating tests at a) room temperature and b) 450 °C. Reproduced from [216].

blended Ti–TiC coatings with 13.8 and 33.4 vol% TiC contents were sprayed on substrates using a Kinetic 4000 gun (CGT Technologies, Germany). N_2 was employed as the carrier gas, the gas pressure was 4 MPa, and the gas temperature was 800 °C. The standoff distance between the substrate and the nozzle exit was set to 40 mm, and the gun traverse speed was fixed at 100 mm/s. Sliding wear tests were performed on the coatings in dry air using a ball-on-flat reciprocating tribometer. Wear tests were conducted using a normal load of 0.5 N, a sliding speed of 3 mm/s, and a track length per cycle of 5 mm, resulting in a total sliding distance of 10 m. The COF of the pure Ti coating fluctuated, remaining in the range of 0.74–1.15. The COF of the Ti–13.8 vol% TiC coating varied from 0.6 to 0.37, whereas the COF of the Ti–34.3 vol% TiC coating exhibited a steady-state value of 0.39 ± 0.01. Both Ti–TiC coatings showed COF values lower than that of the pure Ti coating. A similar tendency was observed for the wear rates. The higher the TiC content, the lower the wear rate. They reported that the addition of TiC did not increase the hardness of the pure Ti coating. Consequently, they concluded that friction and wear behaviours of the coating were controlled by the effect of third bodies, which, as compared to the case of pure Ti, was modified by the addition of TiC. From the study of the wear tracks, they observed that adhesive wear was the dominant wear mechanism in the Ti coating. Because of adhesion forces, the debris agglomerated and formed compact tribofilms. During sliding, repeated plastic deformation and oxidation were noticed. This favoured the incorporation of oxides into the tribolayer and continuous detachment of fragments from the tribolayer, producing small scratches and leading to an abrasive wear mechanism (Fig. 26a). The combination of both wear mechanisms contributed to the high wear rate. For Ti–TiC coatings, the addition of TiC to the Ti matrix substantially decreased the COF and improved the wear resistance of the Ti matrix. They reported that TiC particles provided a hybrid effect, locally reinforcing and providing easy shear. This synergetic effect resulted in a protective tribofilm and improved the wear resistance. The TiC-containing coatings formed compact lubricating tribofilms that led to a stable, reduced friction at higher cycles (Fig. 26b). The high hardness of both composite coatings as compared to that of Ti made them more resistant to plastic deformation. Additionally, the load-bearing capacity of TiC particles and their role in locally reinforcing the Ti matrix against plastic deformation may increase the shear strength and decrease the contact area of the Ti coating with the substrate, increasing the resistance of this coating to adhesive wear.

6.3. *Wear behaviour: Erosion tests*

Aircraft, rockets, and different elements of engines are often subjected to erosion from sand and other solid particles. This phenomenon can cause severe damage and even catastrophic failure. The continuous impact of particles causes the detachment of the material by different processes that generally act in a combined way. Plastic deformation, ploughing, cutting, and cracking are

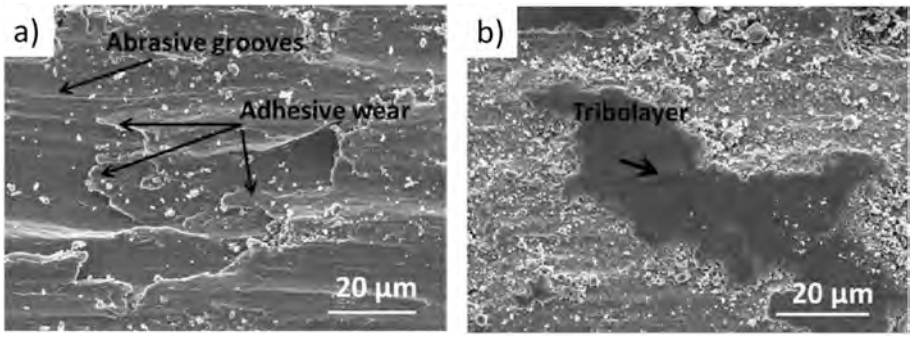

Fig. 26. SE images (10 kV) of the morphologies of the wear tracks of (a) Ti and (b) Ti-33.4 vol% TiC coatings after 1000 sliding cycles. Reproduced from [222].

commonly found to be responsible for the detachment and damage of the material due to the impact of particles during erosion. The contribution of each process to erosion depends on extrinsic and intrinsic parameters. Among the extrinsic parameters, impingement angle, velocity, geometry, size, and density of the erosive particles are important. The intrinsic parameters include properties, such as hardness, fracture toughness, E, yield strength, ductility, and brittleness of the eroding material. Different theoretical models have been proposed to relate these parameters and wear rates during erosion [223–228]. Although these models have been reported by different researchers, they all have certain common features. The erosion rate depends on the velocity affected by an exponent that ranges between 2.0 and 3.0. Wear rates also depend on trigonometric functions of the impingement angle such that ductile metals typically show peak erosion at a shallow impact angle (30°), whereas brittle materials often exhibit maximum wear at normal incidence (90°). Generally, for ductile metals, the higher the hardness, the higher the erosion resistance. Furthermore, for brittle materials, the higher the fracture toughness, the higher the erosion resistance.

6.3.1. *Cold-sprayed Al alloy coatings*

Material removal by erosion is one of the most important damages that can affect Al coatings in the aeronautical sector [229].

Cruz et al. [230] evaluated the erosion performances of Al C355 (Al–Si alloy) coatings cold-sprayed on the same bulk alloy using an upstream system. Air-jet erosion tests were performed on the coatings and the substrate according to the ASTM G76 standard [231]. The Al C355 coatings were processed using two different sets of gas temperature and pressure: 350 °C and 4 MPa (standard conditions) and 500 °C and 6 MPa (enhanced conditions), respectively. Some of the enhanced coatings were heat-treated after spraying (4 h at 150 °C), and finally, several samples of the heat-treated enhanced coatings were anodised. The erosive particles were accelerated by air stream with a pressure of 0.3 MPa through a nozzle towards the testing coupons oriented perpendicular to the spraying direction. The wear rates, Q, were evaluated by the relationship between the mass of the material removed and the mass of the erosive particles striking the surface. Fig. 27 depicts the erosion rates obtained for the substrate, standard coating, enhanced coating, heat-treated enhanced coating, and anodised enhanced coating. The standard coating exhibited the lowest erosion resistance, and its erosion rate was clearly higher than that of the substrate. However, the erosion resistances of the as-sprayed, heat-treated, and anodised heat-treated enhanced coatings were similar to that of the substrate. This indicates that the cold-sprayed Al C355 enhanced coating can be used for repairing the damage caused by erosion. Additionally, no significant effect of anodisation or heat treatment on the erosion behaviour of the enhanced coating was observed.

Residual eroded surfaces of all coatings and the substrate were analysed by SEM (Fig. 28). No signs of cutting were noticed on the damaged surfaces, and signs of ploughing and plastic deformation were observed in all the coatings and the substrate. Consequently, both ploughing and plastic deformation mechanisms were responsible for erosion in all the tested coatings and the substrate. This finding is in agreement with the activation of erosion mechanisms at normal incidence for ductile bulk materials [176,228].

Cruz et al. [230] also determined the erosion coefficient K (Fig. 27b) using the model proposed by Hutchings [176,228,232] for erosion at normal incidence on ductile materials:

$$Q = \frac{K\rho_{Al}\rho_{Al2O3}^{1/2}U^3}{\varepsilon_c^2 H^{3/2}} \tag{15}$$

where ρ_{Al} is the density of the eroded surface (Al C355), ρ_{Al2O3} is the density of the erosive particles (Al_2O_3), U is the velocity of the erosive particles, H is the hardness of the eroded surface, ε_c is the critical plastic strain, and K is a dimensionless factor that represents the severity of erosion. ε_c denotes the threshold deformation from which the detachment of material occurs. A ε_c value of 0.15 was supposed for the Al C355 coatings [233]. The efficiency of erosion was high in the coatings as compared to that in the bulk alloy

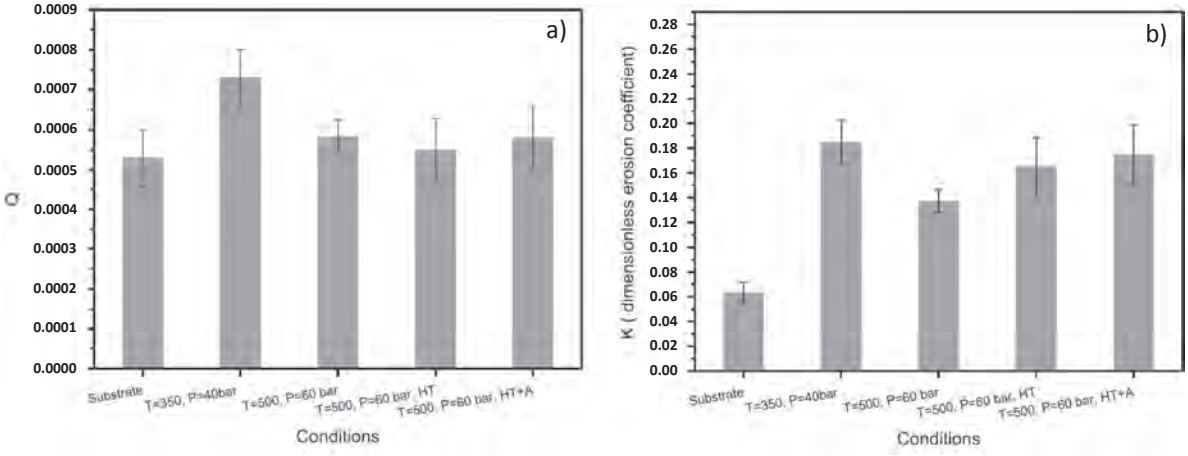

Fig. 27. (a) Erosion rates and (b) dimensionless erosion coefficients for the substrate, standard coating (T = 350, P = 4 MPa), enhanced coating (T = 500, P = 6 MPa) heat treated enhanced coating (T = 500, P = 6 MPa, HT) and anodised enhanced coating (T = 500, P = 6 MPa, HT + A). Reproduced from [230].

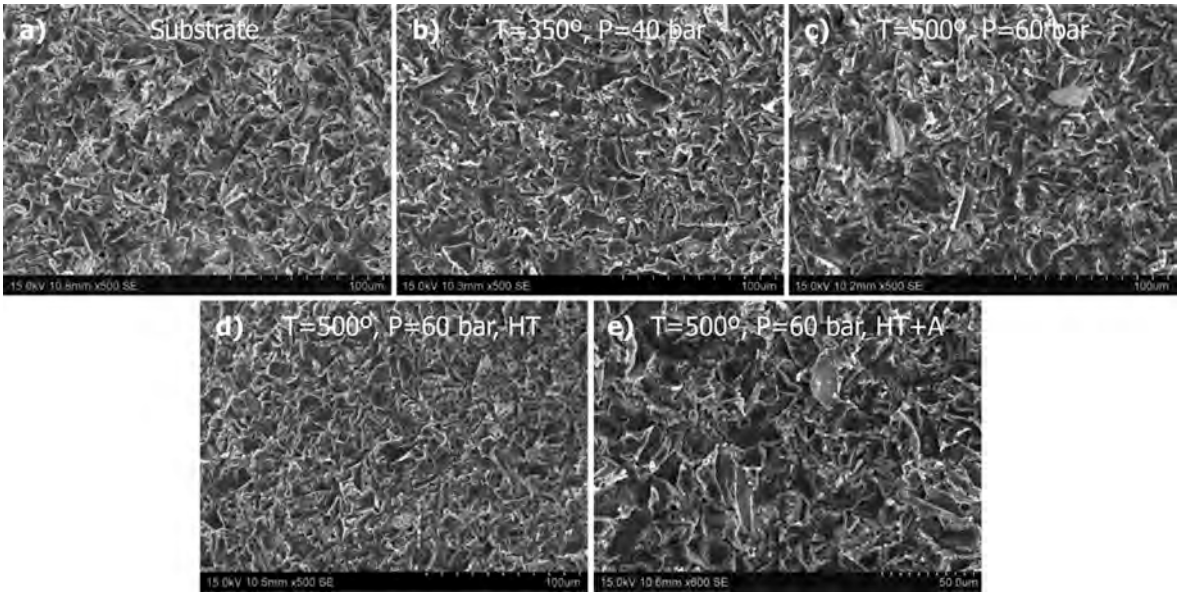

Fig. 28. SEIs showing panoramic views of the eroded surfaces: (a) Substrate, (b) Standard coating, (c) Enhanced coating, (d) Heat treated enhanced coating, and (e) Anodised heat-treated enhanced coating. Reproduced from [230].

(substrate). Among all the coatings, the enhanced coating demonstrated the lowest K (Fig. 27b), indicating a lower efficiency of erosion than those in the cases of the other coatings. Cruz et al. [230] attributed this result to the higher hardness of the enhanced coating.

6.3.2. Cold-sprayed Ti alloy coatings

Similar to Al C355 alloys, Ti6Al4V alloys are extensively used in the components of aeronautical structures. These components experience continuous impact of small particles in suspension. Consequently, erosion has been revealed to be one of the most common damage processes.

Tortuero et al. [234] analysed the wear behaviours of Ti6Al4V coatings by investigating the impact of Al_2O_3 abrasive particles on Ti6Al4V coatings manufactured by HPCS. They compared the responses of the coatings and the bulk alloy and examined the effects of the speeds and the impingement angles of erosive particles on the erosion rate. Herein, two different sets of spraying temperature and pressure were employed to deposit cold-sprayed coatings on Ti6Al4V substrates using N_2: 800 °C and 4 MPa (Ti64-800 °C) and 1100 °C and 5 MPa (Ti64-1100 °C), respectively. Erosion tests were conducted on the coatings using Al_2O_3 particles with an average size of ~50 μm. Erosion tests were also performed on the substrates to obtain a reference value for comparing the wear behaviours of the substrates and the coatings. These tests were conducted at different impingement angles (90 (normal incidence), 60, and 30°) and two impact velocities (70 (±10) and 90 (±17) m/s). Both velocities were measured via two different methods: high-speed photography and a double-disc device [231,234]. During the tests, these velocities were controlled by the pressure of the air that dragged the particles through the nozzle to the surface of the material to be eroded. These pressures were 0.3 and 0.4 MPa for 70 and 90 m/s, respectively. Erosion rates were determined as the ratio of the mass of material removed to the mass of erosive particles, evaluated by sample weight difference before and after testing. By analysing the influence of impingement angle, they found that the substrate and the coatings showed maximum erosion rate at 30°. This rate gradually decreased until 90° (Fig. 29a). This behaviour is characteristic of ductile metals. Another relevant result was the evolution of erosion rate as a function of the carrier gas pressure of erosive particles (Fig. 29b). The higher the carrier gas pressure, the higher the erosion rate. Therefore, the higher the velocity of erosive particles, the higher the erosion rate. This result is in agreement with those of the erosion models, where the erosion rates are proportional to the particle velocity affected by an exponent that ranges between 2.0 and 3.0 [223,224,226–228]. Tortuero et al. [234] performed SEM of the residual imprints of the bulk alloy and the coatings sprayed at a gas temperature and pressure of 1100 °C and 5 MPa, respectively, to determine the corresponding erosion mechanisms.

Residual erosion imprints generated at 30 and 90° on the Ti6Al4V bulk material were characterised by the presence of fragments of Al_2O_3 particles occluded on the eroded surface (Fig. 30a and b). At 30°, cutting and ploughing were identified as the main erosion mechanisms (Fig. 30a). The eroded surface of the Ti6Al4V bulk alloy demonstrated raised-up plastic lips around the local impact areas (Fig. 30b), implying that plastic deformation might be the main erosion mechanism at 90°.

Similar results were obtained from the analysis of residual imprints observed on the cold-sprayed coatings. Residual imprint of the Ti6Al4V coating at 30° was characterised by residual grooves produced by micro-ploughing and micro-cutting (Fig. 30c). However, a piled-up material surrounding the impact prints was noticed in the residual imprint generated at 90°, indicating the existence of plastic deformation as the dominant erosion mechanism (Fig. 30d).

Tortuero et al. [234] also reported that several fragments of erosive particles were embedded in the eroded surface. Because of this

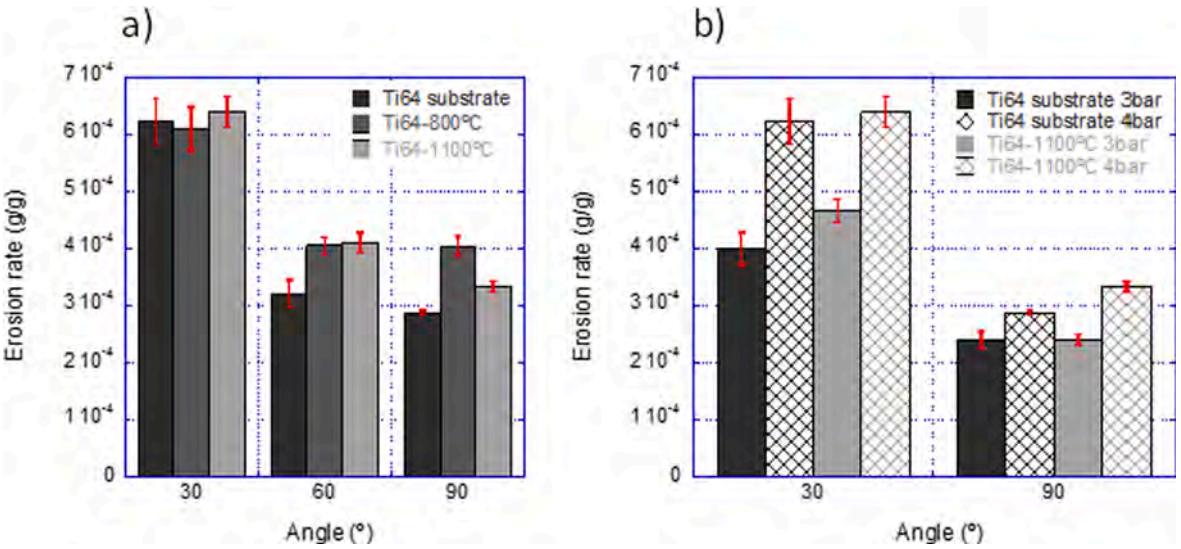

Fig. 29. (a) Erosion rates of Ti6Al4V substrates and coatings versus impingement angles and (b) effect of the inlet air pressure on the erosion rates of Ti6Al4V substrates and coatings versus impingement angles. Reproduced from [234].

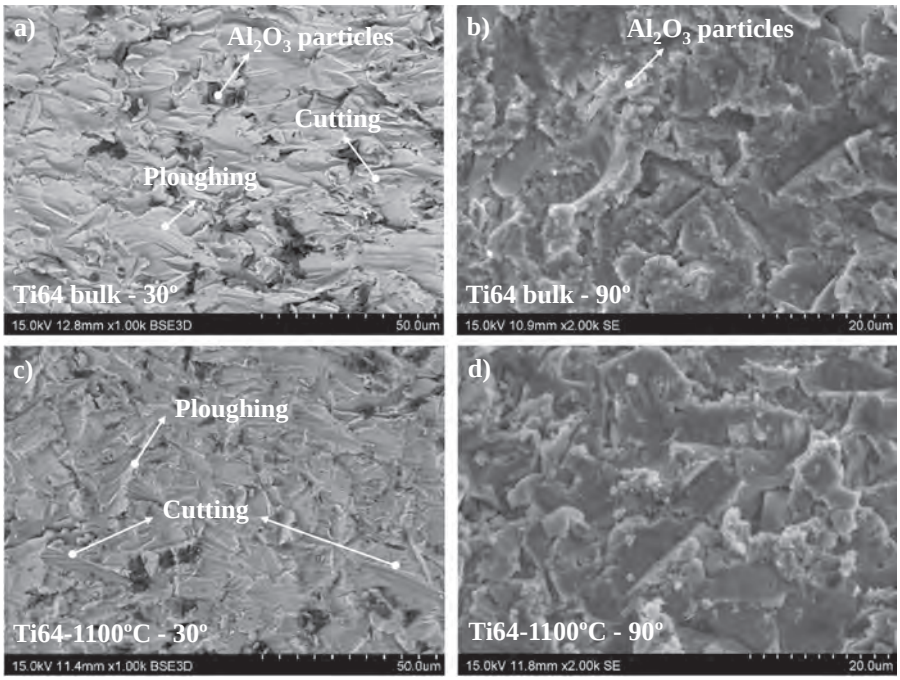

Fig. 30. Representative residual imprints at 0,4 MPa of air pressure. (a) Ti6Al4V bulk alloy at 30°; (b) Ti6Al4V bulk alloy at 90°; (c) Ti6Al4V-1100 °C cold-sprayed coating at 30°; and (d) Ti6Al4V-1100 °C cold-sprayed coating at 90°. Reproduced from [234].

impact, the erosive particles fractured, and some of their fragments occluded on the surface.

7. Conclusions & outlook

The aim of this study was to review the main features of the microstructures and mechanical properties of materials processed by CS deposition and the fundamentals of this technique. CS is a relatively new deposition technique, which can be regarded as a thermal spray technique, with technological advantages over other deposition methods, making it specifically attractive for the maintenance and overhaul of metallic structures in industrial sectors such as aeronautics. The advantages of CS are ascribed to the use of low deposition temperatures, which are always below the melting point of deposited materials. This low processing temperature permits

the deposition of metals on polymers without damaging the soft substrate. The following conclusions were drawn from this review of CS:

- Bonding of the deposited material to the substrate is caused by the high plastic deformation induced in the powder particles at extremely high strain rates. The velocity of powder particles should be higher than V_c. Formation of jetting, where plastic deformation occurs, is mandatory for material adherence. The most extended theory to justify CS bonding is the ASI mechanism. Nevertheless, other explanations related to the interaction of strong pressure waves with the free surface at the particle edges have recently been proposed.
- For CS deposition, two main devices are employed: HPCS and LPCS devices. HPCS devices use upstream injection and operate under high pressure (up to 7 MPa) and temperature (up to 1100 °C) conditions. Although these devices are complex, they enable the deposition of a wide range of materials. LPCS devices utilise downstream injection under low or medium pressures (0.4–3.4 MPa) preheated at a maximum temperature of 550 °C. Although these systems are compact and portable, the achieved powder velocities limit the range of powders that can be deposited.
- Cold-sprayed materials retain the structure of the feedstock powder without oxidation or other undesirable reactions. A splat morphology with different grain structures at the centre and borders of splats is noticed owing to the different levels of plastic deformation. Strain accommodation occurs, inducing microstructural features in the deposited materials. CS allows the deposition of dense coatings with low porosities, which decrease with an increase in particle velocity during spraying.
- Mechanical properties of CS deposits are critical for their technological application. Adhesion and cohesion can be measured by standard methods. Adhesion can be improved by optimising the substrate surface roughness and/or deposition parameters. Although higher impact velocity can improve cohesion, cohesion simultaneously depends on other processing parameters. E and H values of cold-sprayed materials can be evaluated by instrumented indentation. Cold-sprayed materials exhibit higher hardnesses than those of the corresponding powders and bulk alloys due to the plastic deformation induced during deposition.
- Tribological performances of CS deposits are important for the service durability of these deposits. The performance of the sprayed material should be comparable to that of the bulk component if CS is used for restoration.
- Local wear behaviours of the coatings can be evaluated by scratch tests. Scratch tests have been traditionally used to analyse the adhesion strength of coatings, which also provide information about the wear and friction mechanisms. Ploughing, cutting, and chipping can be noticed as material removal mechanisms in cold-sprayed Al and Ti alloys. In each case, the dominant mechanism depends on the processing parameters and subsequent treatments. A careful selection of the processing parameters can lead to cold-sprayed materials with scratch resistances similar to, or even higher than, those of the bulk materials.
- Under dry sliding conditions, wear behaviours can be examined using several test configurations; nevertheless, the most extended configuration is the pin-on-disk test configuration. CS deposition of Al matrix composites leads to coatings with high wear performances when compared with those of the corresponding unreinforced alloys. Under unidirectional and oscillating conditions, the behaviours of cold-sprayed Al and Ti alloys are controlled by plastic deformation, the generation of MML, and, sometimes, by micro-abrasive wear. Again, the wear resistances of cold-sprayed materials can be comparable to those of the bulk materials if the processing conditions are appropriately selected.
- Erosion because of sand or solid particles can cause severe damage to different components as it impacts the surfaces of the components. However, a limited number of studies have been reported on this phenomenon in cold-sprayed materials. The mechanisms responsible for material removal in the cases of cold-sprayed Al and Ti alloys are cutting and ploughing. Ploughing is dominant when the angle of incidence is perpendicular to the coating surface. Erosion rates of cold-sprayed materials can be similar to those of the corresponding bulk materials for some particular deposition parameters.

8. Future perspectives

As reported by Moridi et al. [13] in a review published in 2014, systems that allow plastic deformation can be deposited by CS. Clearly, some coating–substrate combinations offer better results than those of others. To expand the range of materials that can provide reliable cold-sprayed coatings, several future alternatives can be grouped into technological and processing perspectives.

Technological perspectives:

- Designing equipment that increases the range of spraying parameter values and enables spraying at higher temperatures and pressures.
- Designing nozzles that increase the spraying velocities. Optimising the nozzle materials to minimise their wear, guaranteeing a uniform and constant flow of particles for a longer period of time.
- Designing equipment that allows the use of multiple powder feeders, which, in a synchronised way, cause the generation of multilayer coatings at micro- and nano-scales.

Processing perspectives:

- Studying the effect of surface texture characteristics on the adhesion of sprayed particles.
- Investigating the effects of particle size and shape on the adhesion and cohesion of coatings.
- Covering the sprayed particles with films of materials that improve the adhesion and cohesion of coatings.
- Examining alternative consolidation treatments that reduce the porosity of the coatings.

Advancements in these areas will open the possibility of additive manufacturing of new materials via CS.

Declaration of Competing Interest

The authors declare that they have no known competing financial interests or personal relationships that could have appeared to influence the work reported in this paper.

Acknowledgements

This work was financially supported by the European Union's Seventh Framework Programme under grant agreement ACS3-GA-2013-605207 (CORSAIR). The authors would also like to acknowledge the financial support received from the Spanish government CICYT under Grant Nos. MAT2013-41784-R (REMACOLDS) and MAT2016-76928-C2-2-R (DURESPRAY). The authors would also like to acknowledge 'Comunidad de Madrid' and European Structural Funds for their financial support to the ACES2030-CM project (S2018/EMT-4319). The authors are grateful to URJC for its support to the project Cold-SAM.

References

[1] AlMangour B. Fundamentals of cold spray processing: evolution and future perspectives. Cold-Spray Coatings Recent Trends Futur Perspect 2017:3–24. https://doi.org/10.1007/978-3-319-67183-3_1.
[2] Papyrin A, Kosarev V, Klinkov S, Alkhimov A, Fomin VM. Cold Spray Technol 2007. https://doi.org/10.1016/B978-0-08-045155-8.X5000-5.
[3] Botef I, Villafuerte J. Overview. Mod Cold Spray Mater Process Appl; 2015: 1–29. https://doi.org/10.1007/978-3-319-16772-5_1.
[4] Champagne VK. The cold spray materials deposition process: fundamentals and applications; 2007. https://doi.org/10.1533/9781845693787.
[5] Kay CM, Karthikeyan J. High Pressure Cold Spray. ASM International; 2016.
[6] Karthikeyan J. The advantages and disadvantages of the cold spray coating process. Cold Spray Mater Depos Process Fundam Appl 2007:62–71. https://doi.org/10.1533/9781845693787.1.62.
[7] Assadi H, Kreye H, Gärtner F, Klassen T. Cold spraying – a materials perspective. Acta Mater 2016. https://doi.org/10.1016/j.actamat.2016.06.034.
[8] Alkhimov A, Kosarev V, Nesterovich N, Papyrin A. Method of applying coatings. SU 1618778; 1986.
[9] Alkhimov AP, Kosarev VF, Papyrin AN. A method of cold gas-dynamic deposition. Sov Phys Dokl 1990;35:1047–9.
[10] Alkhimov AP, Papyrin AN, Vyazemskogo U, Kosarev VF, Nesterovich NI, Shushpanov MM. Gas-dynamic spraying method for applying a coating. United States Patent. US 5302414; 1994.
[11] Irissou E, Legoux JG, Ryabinin AN, Jodoin B, Moreau C. Review on cold spray process and technology: Part I - Intellectual property. J Therm Spray Technol 2008;17:495–516. https://doi.org/10.1007/s11666-008-9203-3.
[12] Goldbaum D, Poirier D, Irissou E, Legoux JG, Moreau C. Review on cold spray process and technology US patents. Mod Cold Spray Mater Process Appl 2015: 403–29. https://doi.org/10.1007/978-3-319-16772-5_12.
[13] Moridi A, Hassani-Gangaraj SM, Guagliano M, Dao M. Cold spray coating: review of material systems and future perspectives. Surf Eng 2014;30:369–95. https://doi.org/10.1179/1743294414Y.0000000270.
[14] Grigoriev S, Okunkova A, Sova A, Bertrand P, Smurov I. Cold spraying: from process fundamentals towards advanced applications. Surf Coatings Technol 2015;268:77–84. https://doi.org/10.1016/j.surfcoat.2014.09.060.
[15] Chromik RR, Alidokht SA, Shockley JM, Zhang Y. Tribological coatings prepared by cold spray. Cold-Spray Coat 2018:321–48. https://doi.org/10.1007/978-3-319-67183-3_11.
[16] Hassani-Gangaraj SM, Moridi A, Guagliano M. Critical review of corrosion protection by cold spray coatings. Surf Eng 2015;31:803–15. https://doi.org/10.1179/1743294415Y.0000000018.
[17] Koivuluoto H, Vuoristo P. structure and corrosion properties of cold sprayed coatings: a review. Surf Eng 2014;30:404–13. https://doi.org/10.1179/1743294413Y.0000000201.
[18] Bala N, Singh H, Karthikeyan J, Prakash S. Cold spray coating process for corrosion protection: a review. Surf Eng 2014;30:414–21. https://doi.org/10.1179/1743294413Y.0000000148.
[19] Bala N, Singh H. Fundamentals of corrosion mechanisms in cold spray coatings. Cold-Spray Coat 2018:351–71. https://doi.org/10.1007/978-3-319-67183-3_12.
[20] Koivuluoto H. Corrosion resistance of cold-sprayed coatings. Cold-Spray Coat 2018:373–92. https://doi.org/10.1007/978-3-319-67183-3_13.
[21] Dosta S, Cinca N, Vilardell AM, Cano IG, Guilemany JM. Cold spray coatings for biomedical applications. Cold-Spray Coat 2018:533–57. https://doi.org/10.1007/978-3-319-67183-3_19.
[22] Vilardell AM, Cinca N, Concustell A, Dosta S, Cano IG, Guilemany JM. Cold spray as an emerging technology for biocompatible and antibacterial coatings: state of art. J Mater Sci 2015;50. https://doi.org/10.1007/s10853-015-9013-1.
[23] Jeandin M, Koivuluoto H, Vezzu S. Coating properties. Mod Cold Spray Mater Process Appl 2015:107–224. https://doi.org/10.1007/978-3-319-16772-5_4.
[24] Sevillano F, Poza P, Múnez CJ, Vezzù S, Rech S, Trentin A. Cold-sprayed Ni-Al_2O_3 coatings for applications in power generation industry. J Therm Spray Technol 2013;22:772–82. https://doi.org/10.1007/s11666-013-9890-2.
[25] Kong L. High temperature oxidation performance of cold spray coatings. Cold-Spray Coat 2018:393–418. https://doi.org/10.1007/978-3-319-67183-3_14.
[26] Champagne VK, Koh PK, Eden TJ, Wolfe DE, Villafuerte J, Helfritch D. Applications. Mod Cold Spray Mater Process Appl 2015:341–76. https://doi.org/10.1007/978-3-319-16772-5_10.
[27] Cinca N, López E, Dosta S, Guilemany JM. Study of stellite-6 deposition by cold gas spraying. Surf Coatings Technol 2013;232:891–8. https://doi.org/10.1016/j.surfcoat.2013.06.120.
[28] Rubino F, Paradiso V, Astarita A, Carlone P, Squillace A. Advances in titanium on aluminium alloys cold spray coatings. Cold-Spray Coat Recent Trends Futur Perspect 2017:225–49. https://doi.org/10.1007/978-3-319-67183-3_7.
[29] Jahed H, Ghelichi R. Residual stresses and fatigue life enhancement of cold spray. Mod Cold Spray Mater Process Appl 2015:225–52. https://doi.org/10.1007/978-3-319-16772-5_5.
[30] Choi WB, Li L, Luzin V, Neiser R, Gnäupel-Herold T, Prask HJ, et al. Integrated characterization of cold sprayed aluminum coatings. Acta Mater 2007;55: 857–66. https://doi.org/10.1016/j.actamat.2006.09.006.
[31] Ghelichi R, Bagherifard S, Macdonald D, Fernandez-Pariente I, Jodoin B, Guagliano M. Experimental and numerical study of residual stress evolution in cold spray coating. Appl Surf Sci 2014;288:26–33. https://doi.org/10.1016/j.apsusc.2013.09.074.
[32] Shayegan G, Mahmoudi H, Ghelichi R, Villafuerte J, Wang J, Guagliano M, et al. Residual stress induced by cold spray coating of magnesium AZ31B extrusion. Mater Des 2014;60:72–84. https://doi.org/10.1016/j.matdes.2014.03.054.
[33] Jahed H. Residual stresses and fatigue life enhancement of cold spray multiaxial fatigue of lightweight materials view project cold spray coating technology application in lightweighting view project. Springer; 2015:225–52. https://doi.org/10.1007/978-3-319-16772-5_5.

[34] Widener CA, Ozdemir OC, Carter M. Structural repair using cold spray technology for enhanced sustainability of high value assets. Procedia Manuf 2018;21:361–8. https://doi.org/10.1016/j.promfg.2018.02.132.
[35] Petráčková K, Kondás J, Guagliano M. Fixing a hole (with cold spray). Int J Fatigue 2018;110:144–52. https://doi.org/10.1016/j.ijfatigue.2018.01.014.
[36] Yin S, Aldwell B, Lupoi R. Cold spray additive manufacture and component restoration. Cold-Spray Coatings Recent Trends Futur Perspect 2017:195–224. https://doi.org/10.1007/978-3-319-67183-3_6.
[37] Champagne VK, Champagne VK, Widener C. Cold spray applications. Cold-Spray Coatings Recent Trends Futur Perspect 2017:25–56. https://doi.org/10.1007/978-3-319-67183-3_2.
[38] Raoelison RN, Xie Y, Sapanathan T, Planche MP, Kromer R, Costil S, et al. Cold gas dynamic spray technology: a comprehensive review of processing conditions for various technological developments till to date. Addit Manuf 2018;19:134–59. https://doi.org/10.1016/j.addma.2017.07.001.
[39] Bagherifard S, Monti S, Zuccoli MV, Riccio M, Kondás J, Guagliano M. Cold spray deposition for additive manufacturing of freeform structural components compared to selective laser melting. Mater Sci Eng A 2018;721:339–50. https://doi.org/10.1016/j.msea.2018.02.094.
[40] Bagherifard S, Heydari Astaraee A, Locati M, Nawaz A, Monti S, Kondás J, et al. Design and analysis of additive manufacturedbimodal structures obtained by cold spray deposition. Addit Manuf 2020;33. https://doi.org/10.1016/j.addma.2020.101131.
[41] Voyer J, Schulz P, Schreiber M. Electrically conductive flame sprayed aluminum coatings on textile substrates. J Therm Spray Technol 2008;17:818–23. https://doi.org/10.1007/s11666-008-9228-7.
[42] Sampath S. Opportunities for thermal spray in functional materials, electronics, and sensors. Adv Mater Process 2013;171:69–70.
[43] Gonzalez R, Ashrafizadeh H, Lopera A, Mertiny P, McDonald A. A review of thermal spray metallization of polymer-based structures. J Therm Spray Technol 2016;25:897–919. https://doi.org/10.1007/s11666-016-0415-7.
[44] Ganesan A, Affi J, Yamada M, Fukumoto M. Bonding behavior studies of cold sprayed copper coating on the PVC polymer substrate. Surf Coatings Technol 2012;207:262–9. https://doi.org/10.1016/j.surfcoat.2012.06.086.
[45] Ashrafizadeh H, McDonald A, Mertiny P. Deposition of electrically conductive coatings on castable polyurethane elastomers by the flame spraying process. J Therm Spray Technol 2016;25:419–30. https://doi.org/10.1007/s11666-015-0376-2.
[46] Huonnic N, Abdelghani M, Mertiny P, McDonald A. Deposition and characterization of flame-sprayed aluminum on cured glass and basalt fiber-reinforced epoxy tubes. Surf Coatings Technol 2010;205. https://doi.org/10.1016/j.surfcoat.2010.08.029.
[47] Ashari AA, Tucker RC. Thermal spray coatings for fiber reinforced polymer composites. In: Proc. Int. Therm. Spray Conf., vol. 2; 1998.
[48] Petrovicova E, Knight R, Schadler LS, Twardowski TE. Nylon 11/silica nanocomposite coatings applied by the HVOF process. I. Microstructure and morphology. J Appl Polym Sci 2000;77:1684–99. https://doi.org/10.1002/1097-4628(20000822)77:8<1684::AID-APP5>3.0.CO;2-Q.
[49] Strait LH, Jamison RD. Application of PEEK coatings to C/PEEK substrates by plasma-spray process. J Compos Mater 1994;28:211–33. https://doi.org/10.1177/002199839402800302.
[50] Henne RH, Schitter C. Plasma spraying of high performance thermoplastics. In: Berndt C, Sampath S, editors. Adv. Therm. spray Sci. Technol. Proc. 8th Natl. Therm. Spray Conf. Houston: ASM International; 1995. p. 1–795.
[51] Zhou XL, Chen AF, Liu JC, Wu XK, Zhang JS. Preparation of metallic coatings on polymer matrix composites by cold spray. Surf Coat Technol 2011;206:132–6. https://doi.org/10.1016/j.surfcoat.2011.07.005.
[52] Lupoi R, O'Neill W. Deposition of metallic coatings on polymer surfaces using cold spray. Surf Coat Technol 2010;205:2167–73. https://doi.org/10.1016/j.surfcoat.2010.08.128.
[53] Rokni MR, Feng P, Widener CA, Nutt SR. Depositing Al-based metallic coatings onto polymer substrates by cold spray. J Therm Spray Technol 2019;28:1699–708. https://doi.org/10.1007/s11666-019-00911-y.
[54] Gillet V, Aubignat E, Costil S, Courant B, Langlade C, Casari P, et al. Development of low pressure cold sprayed copper coatings on carbon fiber reinforced polymer (CFRP). Surf Coat Technol 2019;364:306–16. https://doi.org/10.1016/j.surfcoat.2019.01.011.
[55] Chen C, Xie X, Xie Y, Yan X, Huang C, Deng S, et al. Metallization of polyether ether ketone (PEEK) by copper coating via cold spray. Surf Coat Technol 2018;342:209–19. https://doi.org/10.1016/j.surfcoat.2018.02.087.
[56] Che H, Chu X, Vo P, Yue • Stephen. Metallization of various polymers by cold spray. J Therm Spray Technol n.d.;27. https://doi.org/10.1007/s11666-017-0663-1.
[57] Liberati AC, Che H, Vo P, Yue S. Observation of an indirect deposition effect while cold spraying Sn-Al mixed powders onto carbon fiber reinforced polymers. J Therm Spray Technol 2020;29:134–46. https://doi.org/10.1007/s11666-019-00967-w.
[58] Affi J, Okazaki H, Yamada M, Fukumoto M. Fabrication of aluminum coating onto CFRP substrate by cold spray. Mater Trans 2011;52:1759–63. https://doi.org/10.2320/matertrans.T-M2011807.
[59] Zhang D, Shipway PH, McCartney DG. Cold gas dynamic spraying of aluminum: the role of substrate characteristics in deposit formation. J Therm Spray Technol 2005;14:109–16. https://doi.org/10.1361/10599630522666.
[60] Ganesan A, Yamada M, Fukumoto M. Cold spray coating deposition mechanism on the thermoplastic and thermosetting polymer substrates. J Therm Spray Technol 2013;22:1275–82. https://doi.org/10.1007/s11666-013-9984-x.
[61] Gardon M, Latorre A, Torrell M, Dosta S, Fernández J, Guilemany JM. Cold gas spray titanium coatings onto a biocompatible polymer. Mater Lett 2013;106:97–9. https://doi.org/10.1016/j.matlet.2013.04.115.
[62] Davis JR. Handbook of thermal spray technology. Materials Park, OH: ASM International; 2004.
[63] Fauchais P, Fukumoto M, Vardelle A, Vardelle M. Knowledge concerning splat formation: an invited review. J Therm Spray Technol 2004;13:337–60. https://doi.org/10.1361/10599630419670.
[64] Bush TB, Khalkhali Z, Champagne V, Schmidt DP, Rothstein JP. Optimization of cold spray deposition of high-density polyethylene powders. J Therm Spray Technol 2017;26:1548–64. https://doi.org/10.1007/s11666-017-0627-5.
[65] Khalkhali Z, Xie W, Champagne VK, Lee JH, Rothstein JP. A comparison of cold spray technique to single particle micro-ballistic impacts for the deposition of polymer particles on polymer substrates. Surf Coat Technol 2018;351:99–107. https://doi.org/10.1016/j.surfcoat.2018.07.053.
[66] Xu Y, Hutchings IM. Cold spray deposition of thermoplastic powder. Surf Coat Technol 2006;201:3044–50. https://doi.org/10.1016/j.surfcoat.2006.06.016.
[67] Shah S, Lee J, Rothstein JP. Numerical simulations of the high-velocity impact of a single polymer particle during cold-spray deposition. J Therm Spray Technol 2017;26:970–84. https://doi.org/10.1007/s11666-017-0557-2.
[68] Ravi K, Ichikawa Y, Deplancke T, Ogawa K, Lame O, Cavaille JY. Development of ultra-high molecular weight polyethylene (UHMWPE) coating by cold spray technique. J Therm Spray Technol 2015;24:1015–25. https://doi.org/10.1007/s11666-015-0276-5.
[69] Assadi H, Gärtner F, Stoltenhoff T, Kreye H. Bonding mechanism in cold gas spraying. Acta Mater 2003;51:4379–94. https://doi.org/10.1016/S1359-6454(03)00274-X.
[70] Grujicic M, Zhao CL, DeRosset WS, Helfritch D. Adiabatic shear instability based mechanism for particles/substrate bonding in the cold-gas dynamic-spray process. Mater Des 2004;25:681–8. https://doi.org/10.1016/j.matdes.2004.03.008.
[71] Perna AS, Astarita A, Carlone P, Guthmann X, Viscusi A. Characterization of cold-spray coatings on fiber-reinforced polymers through nanoindentation tests. Metals (Basel) 2021;11:1–16. https://doi.org/10.3390/met11020331.
[72] Villafuerte J. Modern cold spray: materials, process, and applications; 2015. https://doi.org/10.1007/978-3-319-16772-5.
[73] Cavaliere P. Cold-spray coatings: recent trends and future perspectives; 2017. https://doi.org/10.1007/978-3-319-67183-3.
[74] Viscusi A, Astarita A, Della Gatta R, Rubino F. A perspective review on the bonding mechanisms in cold gas dynamic spray. Surf Eng 2019;35:743–71. https://doi.org/10.1080/02670844.2018.1551768.
[75] Li WY, Zhang DD, Huang CJ, Yin S, Yu M, Wang FF, et al. Modelling of impact behaviour of cold spray particles: review. Surf Eng 2014;30:299–308. https://doi.org/10.1179/1743294414Y.0000000268.
[76] Li W, Cao C, Yin S. Solid-state cold spraying of Ti and its alloys: a literature review. Prog Mater Sci 2020;110:100633. https://doi.org/10.1016/j.pmatsci.2019.100633.

[77] King P, Yandouzi M, Jodoin B. The physics of cold spray. Mod Cold Spray Mater Process Appl 2015:31–72. https://doi.org/10.1007/978-3-319-16772-5_2.
[78] Schmidt T, Gärtner F, Assadi H, Kreye H. Development of a generalized parameter window for cold spray deposition. Acta Mater 2006;54:729–42. https://doi.org/10.1016/j.actamat.2005.10.005.
[79] Klinkov SV, Kosarev VF, Rein M. Cold spray deposition: significance of particle impact phenomena. Aerosp Sci Technol 2005;9:582–91. https://doi.org/10.1016/j.ast.2005.03.005.
[80] Stoltenhoff T, Kreye H, Richter HJ. An analysis of the cold spray process and its coatings. J Therm Spray Technol 2002;11:542–50. https://doi.org/10.1361/105996302770348682.
[81] Schmidt T, Assadi H, Gärtner F, Richter H, Stoltenhoff T, Kreye H, et al. From particle acceleration to impact and bonding in cold spraying. J Therm Spray Technol 2009;18:794–808. https://doi.org/10.1007/s11666-009-9357-7.
[82] Meyer M, Lupoi R. An analysis of the particulate flow in cold spray nozzles. Mech Sci 2015;6:127–36. https://doi.org/10.5194/ms-6-127-2015.
[83] Raoelison RN. Analytical description of solid particles kinematics due to a fluid flow and application to the depiction of characteristic kinematics in cold spraying. Powder Technol 2017;319:191–203. https://doi.org/10.1016/j.powtec.2017.06.029.
[84] Yin S, Meyer M, Li W, Liao H, Lupoi R. Gas flow, particle acceleration, and heat transfer in cold spray: a review. J Therm Spray Technol 2016;25:874–96. https://doi.org/10.1007/s11666-016-0406-8.
[85] Hussain T, McCartney DG, Shipway PH. Impact phenomena in cold-spraying of titanium onto various ferrous alloys. Surf Coat Technol 2011;205:5021–7. https://doi.org/10.1016/j.surfcoat.2011.05.003.
[86] Johnson GR, Cook WH. Fracture characteristics of three metals subjected to various strains, strain rates, temperatures and pressures. Eng Fract Mech 1985;21:31–48. https://doi.org/10.1016/0013-7944(85)90052-9.
[87] Rahmati S, Ghaei A. The use of particle/substrate material models in simulation of cold-gas dynamic-spray process. J Therm Spray Technol 2014;23:530–40. https://doi.org/10.1007/s11666-013-0051-4.
[88] Xie Y, Yin S, Chen C, Planche MP, Liao H, Lupoi R. New insights into the coating/substrate interfacial bonding mechanism in cold spray. Scr Mater 2016;125:1–4. https://doi.org/10.1016/j.scriptamat.2016.07.024.
[89] Kumar S, Bae G, Lee C. Influence of substrate roughness on bonding mechanism in cold spray. Surf Coat Technol 2016;304. https://doi.org/10.1016/j.surfcoat.2016.07.082.
[90] Meng F, Hu D, Gao Y, Yue S, Song J. Cold-spray bonding mechanisms and deposition efficiency prediction for particle/substrate with distinct deformability. Mater Des 2016;109:503–10. https://doi.org/10.1016/j.matdes.2016.07.103.
[91] Ichikawa Y, Tokoro R, Tanno M, Ogawa K. Elucidation of cold-spray deposition mechanism by auger electron spectroscopic evaluation of bonding interface oxide film. Acta Mater 2019;164:39–49. https://doi.org/10.1016/j.actamat.2018.09.041.
[92] Hassani-Gangaraj M, Veysset D, Nelson KA, Schuh CA. In-situ observations of single micro-particle impact bonding. Scr Mater 2018;145:9–13. https://doi.org/10.1016/j.scriptamat.2017.09.042.
[93] Hassani-Gangaraj M, Veysset D, Champagne VK, Nelson KA, Schuh CA. Adiabatic shear instability is not necessary for adhesion in cold spray. Acta Mater 2018;158:430–9. https://doi.org/10.1016/j.actamat.2018.07.065.
[94] Hassani-Gangaraj M, Veysset D, Champagne VK, Nelson KA, Schuh CA. Response to Comment on "Adiabatic shear instability is not necessary for adhesion in cold spray". Scr Mater 2019;162:515–9. https://doi.org/10.1016/j.scriptamat.2018.12.015.
[95] Comment on "Adiabatic shear instability is not necessary for adhesion in cold spray" 2018. https://doi.org/10.1016/j.scriptamat.2018.10.036.
[96] Villafuerte J, Birtch W, Wang J. Commercial cold spray equipment and automation. Mod Cold Spray Mater Process Appl 2015:253–73. https://doi.org/10.1007/978-3-319-16772-5_6.
[97] Koivuluoto H, Coleman A, Murray K, Kearns M, Vuoristo P. High pressure cold sprayed (HPCS) and low pressure cold sprayed (LPCS) coatings prepared from OFHC Cu feedstock: overview from powder characteristics to coating properties. J Therm Spray Technol 2012;21:1065–75. https://doi.org/10.1007/s11666-012-9790-x.
[98] Maev RG, Leshchynsky V. Low-pressure cold spray (LPCS). Cold-Spray Coatings Recent Trends Futur Perspect 2017:95–142. https://doi.org/10.1007/978-3-319-67183-3_4.
[99] Suo X, Yin S, Planche MP, Liu T, Liao H. Strong effect of carrier gas species on particle velocity during cold spray processes. Surf Coat Technol 2015;268:90–3. https://doi.org/10.1016/j.surfcoat.2014.04.039.
[100] Li WY, Zhang C, Guo X, Xu J, Li CJ, Liao H, et al. Ti and Ti-6Al-4V coatings by cold spraying and microstructure modification by heat treatment. Adv Eng Mater 2007;9:418–23. https://doi.org/10.1002/adem.200700022.
[101] Henao J, Concustell A, Cano IG, Cinca N, Dosta S, Guilemany JM. Influence of Cold Gas Spray process conditions on the microstructure of Fe-based amorphous coatings. J Alloys Compd 2015;622:995–9. https://doi.org/10.1016/j.jallcom.2014.11.037.
[102] Sirvent P, Garrido MA, Múnez CJ, Poza P, Vezzù S. Effect of higher deposition temperatures on the microstructure and mechanical properties of Al, 2024 cold sprayed coatings. Surf Coat Technol 2018:337. https://doi.org/10.1016/j.surfcoat.2018.01.055.
[103] Khun NW, Tan AWY, Bi KJW, Liu E. Effects of working gas on wear and corrosion resistances of cold sprayed Ti-6Al-4V coatings. Surf Coat Technol 2016;302:1–12. https://doi.org/10.1016/j.surfcoat.2016.05.052.
[104] Coddet P, Verdy C, Coddet C, Debray F, Lecouturier F. Mechanical properties of thick 304L stainless steel deposits processed by He cold spray. Surf Coat Technol 2015;277:74–80. https://doi.org/10.1016/j.surfcoat.2015.07.001.
[105] Coddet P, Verdy C, Coddet C, Debray F. On the mechanical and electrical properties of copper-silver and copper-silver-zirconium alloys deposits manufactured by cold spray. Mater Sci Eng A 2016;662:72–9. https://doi.org/10.1016/j.msea.2016.03.049.
[106] Liu T, Leazer JD, Brewer LN. Particle deformation and microstructure evolution during cold spray of individual Al-Cu alloy powder particles. Acta Mater 2019;168:13–23. https://doi.org/10.1016/j.actamat.2019.01.054.
[107] MacDonald D, Rahmati S, Jodoin B, Birtch W. An economical approach to cold spray using in-line nitrogen-helium blending. J Therm Spray Technol 2019;28:161–73. https://doi.org/10.1007/s11666-018-0813-0.
[108] Wong W, Irissou E, Ryabinin AN, Legoux JG, Yue S. Influence of helium and nitrogen gases on the properties of cold gas dynamic sprayed pure titanium coatings. J Therm Spray Technol 2011;20:213–26. https://doi.org/10.1007/s11666-010-9568-y.
[109] Balani K, Agarwal A, Seal S, Karthikeyan J. Transmission electron microscopy of cold sprayed 1100 aluminum coating. Scr Mater 2005;53:845–50. https://doi.org/10.1016/j.scriptamat.2005.06.008.
[110] Maev RG, Leshchynsky V. Introduction to low pressure gas dynamic spray: physics & technology; 2008. https://doi.org/10.1002/9783527621903.
[111] Christoulis D, Sarafoglou C. Laser-assisted cold spray. Mod Cold Spray Mater Process Appl 2015:275–302. https://doi.org/10.1007/978-3-319-16772-5_7.
[112] Raoelison RN. Coeval cold spray additive manufacturing variances and innovative contributions. Cold-Spray Coatings Recent Trends Futur Perspect 2017:57–94. https://doi.org/10.1007/978-3-319-67183-3_3.
[113] Christoulis DK, Jeandin M, Irissou E, Legoux J-G, Knapp W. Laser-Assisted Cold Spray (LACS). Nd YAG Laser 2012. https://doi.org/10.5772/36104.
[114] Kulmala M, Vuoristo P. Influence of process conditions in laser-assisted low-pressure cold spraying. Surf Coat Technol 2008;202:4503–8. https://doi.org/10.1016/j.surfcoat.2008.04.034.
[115] Birt AM, Champagne VK, Sisson RD, Apelian D. Statistically guided development of laser-assisted cold spray for microstructural control of Ti-6Al-4V. Metall Mater Trans A Phys Metall Mater Sci 2017;48:1931–43. https://doi.org/10.1007/s11661-017-3970-8.
[116] Bray M, Cockburn A, O'Neill W. The Laser-assisted Cold Spray process and deposit characterisation. Surf Coat Technol 2009;203:2851–7. https://doi.org/10.1016/j.surfcoat.2009.02.135.
[117] Poza P, Múnez CJ, Garrido-Maneiro MA, Vezzù S, Rech S, Trentin A. Mechanical properties of Inconel 625 cold-sprayed coatings after laser remelting. Depth sensing indentation analysis. Surf Coat Technol 2014;243. https://doi.org/10.1016/j.surfcoat.2012.03.018.
[118] Marrocco T, Hussain T, McCartney DG, Shipway PH. Corrosion performance of laser posttreated cold sprayed titanium coatings. J Therm Spray Technol 2011;20:909–17. https://doi.org/10.1007/s11666-011-9637-x.

[119] Reza Rokni M, Nutt SR, Widener CA, Crawford GA, Champagne VK. Structure-properties relations in high-pressure cold-sprayed deposits. Cold-Spray Coatings Recent Trends Futur Perspect 2017:143–92. https://doi.org/10.1007/978-3-319-67183-3_5.
[120] Lee C, Kim J. Microstructure of kinetic spray coatings: a review. J Therm Spray Technol 2015;24:592–610. https://doi.org/10.1007/s11666-015-0223-5.
[121] Cinca N, Rebled JM, Estradé S, Peiró F, Fernández J, Guilemany JM. Influence of the particle morphology on the Cold Gas Spray deposition behaviour of titanium on aluminum light alloys. J Alloys Compd 2013;554:89–96. https://doi.org/10.1016/j.jallcom.2012.11.069.
[122] Jeandin M, Rolland G, Descurninges LL, Berger MH. Which powders for cold spray? Surf Eng 2014;30:291–8. https://doi.org/10.1179/1743294414Y.0000000253.
[123] Kim KH, Watanabe M, Kawakita J, Kuroda S. Grain refinement in a single titanium powder particle impacted at high velocity. Scr Mater 2008;59:768–71. https://doi.org/10.1016/j.scriptamat.2008.06.020.
[124] McCune RC, Donlon WT, Popoola OO, Cartwright EL. Characterization of copper layers produced by cold gas-dynamic spraying. J Therm Spray Technol 2000;9:73–82. https://doi.org/10.1361/105996300770350087.
[125] Rokni MR, Nutt SR, Widener CA, Champagne VK, Hrabe RH. Review of relationship between particle deformation, coating microstructure, and properties in high-pressure cold spray. J Therm Spray Technol 2017;26:1308–55. https://doi.org/10.1007/s11666-017-0575-0.
[126] Cortés R, Garrido MA, Rico A, Múnez CJ, Poza P, Martos AM, et al. Effect of processing conditions on the mechanical performance of stainless steel cold sprayed coatings. Surf Coat Technol 2020;394:125874. https://doi.org/10.1016/j.surfcoat.2020.125874.
[127] ASTM C633-13. Standard Test Method for Adhesion or Cohesion Strength of Thermal Spray Coatings; 2017.
[128] Legoux Jean-Gabriel, Irissou Eric, Perton M, Poitier D, Blouin A, Costil S, et al. Cold sprayed Ti-6Al-4V coating adhesion and cohesion strength enhancement by surface preparation optimization. In: Int. Therm. Spray Conf. Expo. 2012; 2012.
[129] Sabard A, McNutt P, Begg H, Hussain T. Cold spray deposition of solution heat treated, artificially aged and naturally aged Al 7075 powder. Surf Coat Technol 2020;385. https://doi.org/10.1016/j.surfcoat.2020.125367.
[130] Goldbaum D, Shockley JM, Chromik RR, Rezaeian A, Yue S, Legoux JG, et al. The effect of deposition conditions on adhesion strength of Ti and Ti6Al4V cold spray splats. J Therm Spray Technol 2012;21:288–303. https://doi.org/10.1007/s11666-011-9720-3.
[131] Perton M, Costil S, Wong W, Poirier D, Irissou E, Legoux JG, et al. Effect of pulsed laser ablation and continuous laser heating on the adhesion and cohesion of cold sprayed Ti-6Al-4V coatings. J Therm Spray Technol 2012;21:1322–33. https://doi.org/10.1007/s11666-012-9812-8.
[132] Binder K, Gottschalk J, Kollenda M, Gärtner F, Klassen T. Influence of impact angle and gas temperature on mechanical properties of titanium cold spray deposits. J Therm Spray Technol 2011;20:234–42. https://doi.org/10.1007/s11666-010-9557-1.
[133] Oliver WC, Pharr GM. An improved technique for determining hardness and elastic modulus using load and displacement sensing indentation experiments. J Mater Res 1992;7:1564–83. https://doi.org/10.1557/JMR.1992.1564.
[134] Rokni MR, Widener CA, Champagne VK, Crawford GA, Nutt SR. The effects of heat treatment on 7075 Al cold spray deposits. Surf Coat Technol 2017;310:278–85. https://doi.org/10.1016/j.surfcoat.2016.10.064.
[135] Chavan NM, Ramakrishna M, Phani PS, Rao DS, Sundararajan G. The influence of process parameters and heat treatment on the properties of cold sprayed silver coatings. Surf Coat Technol 2011;205:4798–807. https://doi.org/10.1016/j.surfcoat.2011.04.063.
[136] Garrido MA, Sirvent P, Poza P. Evaluation of mechanical properties of Ti6Al4V cold sprayed coatings*. Surf Eng 2017. https://doi.org/10.1080/02670844.2017.1398442.
[137] Tan AWY, Sun W, Bhowmik A, Lek JY, Marinescu I, Li F, et al. Effect of coating thickness on microstructure, mechanical properties and fracture behaviour of cold sprayed Ti6Al4V coatings on Ti6Al4V substrates. Surf Coat Technol 2018;349:303–17. https://doi.org/10.1016/j.surfcoat.2018.05.060.
[138] Goldbaum D, Chromik RR, Yue S, Irissou E, Legoux JG. Mechanical property mapping of cold sprayed Ti splats and coatings. J Therm Spray Technol 2011;20:486–96. https://doi.org/10.1007/s11666-010-9546-4.
[139] Bhattiprolu VS, Johnson KW, Ozdemir OC, Crawford GA. Influence of feedstock powder and cold spray processing parameters on microstructure and mechanical properties of Ti-6Al-4V cold spray depositions. Surf Coat Technol 2018;335:1–12. https://doi.org/10.1016/j.surfcoat.2017.12.014.
[140] Bin S, Shufeng LI, Hisashi I, Umeda J, Katsuyoshi K. Oxygen solid solution strengthened pure titanium powder materials. Trans JWRI 2012;41:59–64.
[141] Campbell JP, Astarita A, Viscusi A, Saha GC. Investigation of strain-hardening characteristics of cold-sprayed Al–Al2O3 coatings: a combined nanoindentation and expanding cavity models approach. Surf Eng 2020;36:1022–31. https://doi.org/10.1080/02670844.2019.1620438.
[142] Sousa B, Sundberg K, Massar C, Champagne Jr V, Cote D. Spherical nanomechanical characterization of novel nanocrystalline Cu cold spray manufactured materials. In: APS March Meet. Abstr., vol. 2019; 2019.
[143] Pathak S, Kalidindi SR. Spherical nanoindentation stress-strain curves. Mater Sci Eng R Reports 2015;91:1–36. https://doi.org/10.1016/j.mser.2015.02.001.
[144] Leitner A, Maier-Kiener V, Kiener D. Essential refinements of spherical nanoindentation protocols for the reliable determination of mechanical flow curves. Mater Des 2018;146:69–80. https://doi.org/10.1016/j.matdes.2018.03.003.
[145] Dean J, Wheeler JM, Clyne TW. Use of quasi-static nanoindentation data to obtain stress-strain characteristics for metallic materials. Acta Mater 2010;58:3613–23. https://doi.org/10.1016/j.actamat.2010.02.031.
[146] Basu S, Moseson A, Barsoum MW. On the determination of spherical nanoindentation stress-strain curves. J Mater Res 2006;21:2628–37. https://doi.org/10.1557/jmr.2006.0324.
[147] Cortés R, Garrido MÁ, Poza P, Martos A, Dosta S, García I. Cold sprayed coatings for repairing damaged metallic structures. Key Eng Mater 2019;813 KEM:74–9. https://doi.org/10.4028/www.scientific.net/KEM.813.74.
[148] Viscusi A, Durante M, Astarita A, Boccarusso L, Carrino L, Perna AS. Experimental evaluation of metallic coating on polymer by cold spray. Procedia Manuf 2020;47:761–5. https://doi.org/10.1016/j.promfg.2020.04.232.
[149] Shockley JM, Descartes S, Vo P, Irissou E, Chromik RR. The influence of Al2O3 particle morphology on the coating formation and dry sliding wear behavior of cold sprayed Al-Al2O3 composites. Surf Coat Technol 2015;270:324–33. https://doi.org/10.1016/j.surfcoat.2015.01.057.
[150] Champagne VK. The repair of magnesium rotorcraft components by cold spray. J Fail Anal Prev 2008;8:164–75. https://doi.org/10.1007/s11668-008-9116-y.
[151] Stoltenhoff T, Zimmermann F. Cold spray coatings for aluminum aerospace components exposed to high dynamic stresses. In: Proc. 8th HVOF Kolloquim Erding 5-6 Novemb. 200; 2009. p. 135–43.
[152] Kumar S, Chavan N. Cold Spray Coating Technology: Activities at ARCI, briefing; 2011.
[153] Valli J, Mäkelä U. Applications of the scratch test method for coating adhesion assessment. Wear 1987;115:215–21. https://doi.org/10.1016/0043-1648(87)90211-0.
[154] Valli J. A review of adhesion test methods for thin hard coatings. J Vac Sci Technol A Vacuum, Surfaces, Film 1986;4:3007–14. https://doi.org/10.1116/1.573616.
[155] Sekler J, Steinmann PA, Hintermann HE. The scratch test: different critical load determination techniques. Surf Coat Technol 1988;36:519–29. https://doi.org/10.1016/0257-8972(88)90179-X.
[156] Hedenqvist P, Hogmark S. Experiences from scratch testing of tribological PVD coatings. Tribol Int 1997;30:507–16. https://doi.org/10.1016/s0301-679x(97)00014-5.
[157] Steinmann PA, Tardy Y, Hintermann HE. Adhesion testing by the scratch test method: the influence of intrinsic and extrinsic parameters on the critical load. Thin Solid Films 1987;154:333–49. https://doi.org/10.1016/0040-6090(87)90377-4.
[158] Burnett PJ, Rickerby DS. The relationship between hardness and scratch adhesion. Thin Solid Films 1987;154:403–16. https://doi.org/10.1016/0040-6090(87)90382-8.
[159] Rickerby DS. A review of the methods for the measurement of coating-substrate adhesion. Surf Coat Technol 1988;36:541–57. https://doi.org/10.1016/0257-8972(88)90181-8.
[160] Bhushan B, Gupta BK, Azarian MH. Nanoindentation, microscratch, friction and wear studies of coatings for contact recording applications. Wear 1995;181–183:743–58. https://doi.org/10.1016/0043-1648(95)90191-4.

[161] prEN1071-3. Advanced Technical Ceramics-Methods of Tests for Ceramic Coatings. Part 3. Determination of Adhesion and Other Mechanical Failure Modes by Scratch Test. 1999. Test 1999.
[162] Bull SJ, Rickerby DS. Failure modes in scratch adhesion testing: some observations. In: Sudarshan TS, Bhat DG, editors. Surf. Modif. Technol. 111; 1990.
[163] Bull SJ. Failure modes in scratch adhesion testing. Surf Coat Technol 1991;50:25–32. https://doi.org/10.1016/0257-8972(91)90188-3.
[164] Bhushan B. Modern tribology handbook. CRC Press; 2001.
[165] Kayaba T. The latest investigations of wear by the microscopic observations. JSLE Trans 1984;29:9–14.
[166] Benjamin P, Weaver C. Adhesion of metal films to glass. Proc R Soc London Ser A, Math Phys Sci 1959;254:177–83.
[167] Mittal KL. Adhesion measurement of thin films. Electrocompon Sci Technol 1976;3:21–42. https://doi.org/10.1155/APEC.3.21.
[168] Laugier MT. An energy approach to the adhesion of coatings using the scratch test. Thin Solid Films 1984;117:243–9. https://doi.org/10.1016/0040-6090(84)90354-7.
[169] Laugier MT. Adhesion of TiC and TiN coatings prepared by chemical vapour deposition on WC-Co-based cemented carbides. J Mater Sci 1986;21:2269–72. https://doi.org/10.1007/BF01114266.
[170] Bull SJ, Rickerby DS, Matthews A, Leyland A, Pace AR, Valli J. The use of scratch adhesion testing for the determination of interfacial adhesion: the importance of frictional drag. Surf Coat Technol 1988;36:503–17. https://doi.org/10.1016/0257-8972(88)90178-8.
[171] Stroud MF, Wilman H. The proportion of the groove volume removed as wear in abrasion of metals. Br J Appl Phys 1962;13:173–8. https://doi.org/10.1088/0508-3443/13/4/312.
[172] Zum Gahr KH, Mewes D. Severity of material removal in abrasive wear of ductile metals. In: Wear Mater. Int. Conf. Wear Mater.; 1983.
[173] Pitchuka SB, Lahiri D, Sundararajan G, Agarwal A. Scratch-induced deformation behavior of cold-sprayed aluminum amorphous/nanocrystalline coatings at multiple load scales. J Therm Spray Technol 2014;23:502–13. https://doi.org/10.1007/s11666-013-0021-x.
[174] Chen Y, Bakshi SR, Agarwal A. Correlation between nanoindentation and nanoscratch properties of carbon nanotube reinforced aluminum composite coatings. Surf Coat Technol 2010;204:2709–15. https://doi.org/10.1016/j.surfcoat.2010.02.024.
[175] Sirvent P, Garrido-Maneiro MÁ, Poza P. Influence of processing parameters on the local scratch resistance of cold sprayed Ti6Al4V coatings. Key Eng Mater 2019. https://doi.org/10.4028/www.scientific.net/KEM.813.92.
[176] Hutchings I, Shipway P. Tribology: Friction and wear of engineering materials: 2nd ed.; 2017.
[177] Archard JF, Hirst W. The wear of metals under unlubricated conditions. Proc R Soc London Ser A Math Phys Sci 1956;236:397–410. https://doi.org/10.1098/rspa.1956.0144.
[178] Argibay N, Chandross M, Cheng S, Michael JR. Linking microstructural evolution and macro-scale friction behavior in metals. J Mater Sci 2017;52:2780–99. https://doi.org/10.1007/s10853-016-0569-1.
[179] Holmberg K, Matthews A. Coatings tribology: properties, mechanisms, techniques and applications in surface engineering; 2009.
[180] Erdemir A, Voevodin AA. Nanocomposite Coatings for Severe Applications. Handb. Depos. Technol. Film. Coatings; 2010. p. 679–715. https://doi.org/10.1016/B978-0-8155-2031-3.00014-4.
[181] Sato A, Mehrabian R. Aluminum matrix composites: fabrication and properties. Metall Trans B 1976;7:443–51. https://doi.org/10.1007/BF02652716.
[182] Lee HY, Yu YH, Lee YC, Hong YP, Ko KH. Cold spray of SiC and Al2O3 with soft metal incorporation: a technical contribution. J Therm Spray Technol 2004;13:184–9. https://doi.org/10.1361/10599630419355.
[183] Sova A, Kosarev VF, Papyrin A, Smurov I. Effect of ceramic particle velocity on cold spray deposition of metal-ceramic coatings. J Therm Spray Technol 2011;20:285–91. https://doi.org/10.1007/s11666-010-9571-3.
[184] Sova A, Papyrin A, Smurov I. Influence of ceramic powder size on process of cermet coating formation by cold spray. J Therm Spray Technol 2009;18:633–41. https://doi.org/10.1007/s11666-009-9359-5.
[185] Chung S, Hwang BH. A microstructural study of the wear behaviour of SiCp/Al composites. Tribol Int 1994;27:307–14. https://doi.org/10.1016/0301-679X(94)90024-8.
[186] Irissou E, Legoux JG, Arsenault B, Moreau C. Investigation of Al-Al 2O 3 cold spray coating formation and properties. J Therm Spray Technol 2007;16:661–8. https://doi.org/10.1007/s11666-007-9086-8.
[187] Spies HJ. Surface engineering of aluminium and titanium alloys: An overview. Surf Eng 2010;26:126–34. https://doi.org/10.1179/174329409X451146.
[188] Clyne TW, Withers PJ. An Introduction to Metal Matrix Composites; 1993. https://doi.org/10.1017/cbo9780511623080.
[189] Deuis RL, Subramanian C, Yellup JM. Dry sliding wear of aluminium composites – a review. Compos Sci Technol 1997;57:415–35. https://doi.org/10.1016/S0266-3538(96)00167-4.
[190] Venkataraman B, Sundararajan G. The sliding wear behaviour of Al-SiC particulate composites – I. Macrobehaviour. Acta Mater 1996;44:451–60. https://doi.org/10.1016/1359-6454(95)00217-0.
[191] Alpas AT, Zhang J. Effect of microstructure (particulate size and volume fraction) and counterface material on the sliding wear resistance of particulate-reinforced aluminum matrix composites. Metall Mater Trans A 1994;25:969–83. https://doi.org/10.1007/BF02652272.
[192] Rohatgi PK, Yarandi FM, Liu Y. Influence of solidification conditions on segregation of aluminum-silicon carbide particle composites. In: Fishman SG, Dhingra AK, editors. Proc. Int. Symp. Adv. Cast Reinf. Met. Compos.; 1988. p. 249–55.
[193] Nemati N, Emamy M, Penkov OV, Kim J, Kim DE. Mechanical and high temperature wear properties of extruded Al composite reinforced with Al13Fe4 CMA nanoparticles. Mater Des 2016;90:532–44. https://doi.org/10.1016/j.matdes.2015.11.001.
[194] Tiryakioğlu M, Campbell J. Guidelines for designing metal casting research: application to aluminium alloy castings. Int J Cast Met Res 2007;20:25–9. https://doi.org/10.1179/136404607X186509.
[195] Sajjadi SA, Ezatpour HR, Beygi H. Microstructure and mechanical properties of Al-Al_2O_3 micro and nano composites fabricated by stir casting. Mater Sci Eng A 2011;528:8765–71. https://doi.org/10.1016/j.msea.2011.08.052.
[196] Miller WS, Zhuang L, Bottema J, Wittebrood AJ, De Smet P, Haszler A, et al. Recent development in aluminium alloys for the automotive industry. Mater Sci Eng A 2000;280:37–49. https://doi.org/10.1016/S0921-5093(99)00653-X.
[197] Brown KR, Venie MS, Woods RA. Increasing use of aluminum in automotive applications. JOM 1995;47:20–3. https://doi.org/10.1007/BF03221224.
[198] Gaitonde VN, Karnik SR, Jayaprakash MS. Some studies on wear and corrosion properties of Al5083/Al2O3/Graphite hybrid composites. J Miner Mater Charact Eng 2012;2012.
[199] Kozma M. Friction and wear of metal matrix composites. Natl. Tribol. Conf.; 2003. p. 99–106.
[200] Ravi Kumar K, Mohanasundaram KM, Arumaikkannu G, Subramanian R. Analysis of parameters influencing wear and frictional behavior of aluminum-fly ash composites. Tribol Trans 2012;55:723–9. https://doi.org/10.1080/10402004.2012.700763.
[201] Zhang L, He XB, Qu XH, Duan BH, Lu X, Qin ML. Dry sliding wear properties of high volume fraction SiCp/Cu composites produced by pressureless infiltration. Wear 2008;265:1848–56. https://doi.org/10.1016/j.wear.2008.04.029.
[202] Kim HJ, Windl W, Rigney D. Structure and chemical analysis of aluminum wear debris: experiments and ab initio simulations. Acta Mater 2007;55:6489–98. https://doi.org/10.1016/j.actamat.2007.08.013.
[203] Cruz D, Garrido MÁ, Rico Á, Múnez CJ, Poza P. Wear resistance of cold sprayed Al alloys for aeronautical repairs. Surf Eng 2018. https://doi.org/10.1080/02670844.2018.1427318.
[204] Spencer K, Fabijanic DM, Zhang MX. The use of Al-Al_2O_3 cold spray coatings to improve the surface properties of magnesium alloys. Surf Coat Technol 2009;204:336–44. https://doi.org/10.1016/j.surfcoat.2009.07.032.
[205] Tao Y, Xiong T, Sun C, Jin H, Du H, Li T. Effect of α-Al_2O_3 on the properties of cold sprayed Al/α-Al 2 O 3 composite coatings on AZ91D magnesium alloy. Appl Surf Sci 2009;256:261–6. https://doi.org/10.1016/j.apsusc.2009.08.012.
[206] Shockley JM, Strauss HW, Chromik RR, Brodusch N, Gauvin R, Irissou E, et al. In situ tribometry of cold-sprayed Al-Al_2O_3 composite coatings. Surf Coat Technol 2013;215:350–6. https://doi.org/10.1016/j.surfcoat.2012.04.099.

[207] Shockley JM, Descartes S, Irissou E, Legoux JG, Chromik RR. Third body behavior during dry sliding of cold-sprayed Al-Al_2O_3 composites: In situ tribometry and microanalysis. Tribol Lett 2014;54:191–206. https://doi.org/10.1007/s11249-014-0326-z.
[208] Wang Y, Rainforth WM, Jones H, Lieblich M. Dry wear behaviour and its relation to microstructure of novel 6092 aluminium alloy-Ni_3Al powder metallurgy composite. Wear 2001;250:1421–32. https://doi.org/10.1016/S0043-1648(01)00783-9.
[209] Wu J, Tao Y, Jin H, Li M, Xiong T, Sun C. Friction and wear properties of cold gas dynamic sprayed α-Al_2O_3-Al composite coatings. J Coat 2013;2013:1–7. https://doi.org/10.1155/2013/613178.
[210] Khun NW, Tan AWY, Liu E. Mechanical and tribological properties of cold-sprayed Ti coatings on Ti-6Al-4V substrates. J Therm Spray Technol 2016;25:715–24. https://doi.org/10.1007/s11666-016-0396-6.
[211] Khun NW, Tan AWY, Sun W, Liu E. Wear and corrosion resistance of thick Ti-6Al-4V coating deposited on Ti-6Al-4V substrate via high-pressure cold spray. J Therm Spray Technol 2017;26:1393–407. https://doi.org/10.1007/s11666-017-0588-8.
[212] Sirvent P, Garrido MA, Lozano-Perez S, Poza P. Oscillating and unidirectional sliding wear behaviour of cold sprayed Ti-6Al-4V coating on Ti-6Al-4V substrate. Surf Coat Technol 2020. https://doi.org/10.1016/j.surfcoat.2019.125152.
[213] DIN 50324. Testing of friction and wear model test for sliding friction of solids (ball on disc system); 1992.
[214] ASTM G99. Standard test method for wear testing with a pin-on-disk apparatus; 2017.
[215] Attia H, Meshreki M, Korashy A, Thomson V, Chung V. Fretting wear characteristics of cold gas-dynamic sprayed aluminum alloys. Tribol Int 2011;44:1407–16. https://doi.org/10.1016/j.triboint.2011.05.006.
[216] Poza P, Sirvent P, Rico Á, Múnez CJ, Garrido MÁ. Oscillating contact wear in cold sprayed Ti6AlV coatings for aeronautical repairs. Mater Sci Forum 2018;941 MSF:1686–91. https://doi.org/10.4028/www.scientific.net/MSF.941.1686.
[217] Siva Rama Krishna D, Brama YL, Sun Y. Thick rutile layer on titanium for tribological applications. Tribol Int 2007;40:329–34. https://doi.org/10.1016/j.triboint.2005.08.004.
[218] Dalili N, Edrisy A, Farokhzadeh K, Li J, Lo J, Riahi AR. Improving the wear resistance of Ti-6Al-4V/TiC composites through thermal oxidation (TO). Wear 2010;269:590–601. https://doi.org/10.1016/j.wear.2010.06.006.
[219] Kim K, Geringer J. Analysis of energy dissipation in fretting corrosion experiments with materials used as hip prosthesis. Wear 2012;296:497–503. https://doi.org/10.1016/j.wear.2012.07.014.
[220] Sun Y. Thermally oxidised titanium coating on aluminium alloy for enhanced corrosion resistance. Mater Lett 2004;58:2635–9. https://doi.org/10.1016/s0167-577x(04)00240-x.
[221] Sun Y. Tribological rutile-TiO_2 coating on aluminium alloy. Appl Surf Sci 2004;233:328–35. https://doi.org/10.1016/j.apsusc.2004.03.241.
[222] Alidokht SA, Munagala VNV, Chromik RR. Role of third bodies in friction and wear of cold-sprayed Ti and Ti–TiC composite coatings. Tribol Lett 2017;65. https://doi.org/10.1007/s11249-017-0899-4.
[223] Finnie I. Erosion of surfaces by solid particles. Wear 1960;3:87–103. https://doi.org/10.1016/0043-1648(60)90055-7.
[224] Bitter JGA. A study of erosion phenomena part I. Wear 1963;6:5–21. https://doi.org/10.1016/0043-1648(63)90003-6.
[225] Bitter JGA. A study of erosion phenomena Part II. Wear 1963;6:169–90. https://doi.org/10.1016/0043-1648(63)90073-5.
[226] Neilson JH, Gilchrist A. Erosion by a stream of solid particles. Wear 1968;11:111–22. https://doi.org/10.1016/0043-1648(68)90591-7.
[227] Hashish M. Modified model for erosion. In: Proc. 7th Int. Conf. Eros. by Liq. solid impact, Cambridge, UK; 1987. p. 461–80.
[228] Hutchings IM. Mechanisms of the erosion of metals by solid particles. ASTM STP 664 1979:59–76. https://doi.org/10.1520/stp35795s.
[229] Prasad N, Wanhill R. Aerospace materials and material technologies; 2017.
[230] Cruz D, Garrido MA, Múnez CJ, Rico A, Poza P. Erosion of cold sprayed aeronautical coatings. Surf Eng 2019;35:792–800. https://doi.org/10.1080/02670844.2019.1586096.
[231] ASTM G76 - 18. Standard Test Method for Conducting Erosion Tests by Solid Particle Impingement Using Gas Jets; 2018.
[232] Hutchings IM. A model for the erosion of metals by spherical particles at normal incidence. Wear 1981;70:269–81. https://doi.org/10.1016/0043-1648(81)90347-1.
[233] Levin BF, Vecchio KS, DuPont JN, Marder AR. Modeling solid-particle erosion of ductile alloys. Metall Mater Trans A Phys Metall Mater Sci 1999;30:1763–74. https://doi.org/10.1007/s11661-999-0175-9.
[234] Tortuero S, Garrido MA, Poza P, Rodríguez J. Evaluating the erosion resistance of Ti6Al4V coatings deposited by cold spray. Wear 2020;454–455:2033–7. https://doi.org/10.1016/j.wear.2020.203337.